Geophysical Prospecting, 2006, **54**, 211–236

The origin and nature of seismic reflections of sharp-based shoreface deposits (upper Jurassic Siliciclastics, northern France)

H. Braaksma,[1]* G.G. Drijkoningen,[2] N. Filippidou,[2] J.A.M. Kenter[3] and J.N. Proust[4]

[1]*Laboratoire de Tectonophysique – cc56, Université Montpellier 2, Place Eugene Bataillon 34095 Montpellier – Cedex 5, France,* [2]*Delft University of Technology, Delft, the Netherlands,* [3]*Faculty of Earth and Life Sciences, Vrije Universiteit Amsterdam, the Netherlands,* [4]*UMR CNRS 6118 Geosciences Rennes, France*

Received April 2005, revision accepted September 2005

ABSTRACT

In order to advance understanding of the relationship between geological properties and their physical expression in reflection images, this study has focused expertise in reflection geophysics, petrophysics and sedimentology on the same geological object, in this case a succession of Upper Jurassic sharp-based shoreface deposits embedded in offshore marine shales in northern France. This integrated approach to determine firstly the origin and nature of seismic reflections (calibration) and secondly to provide a means of extracting geological information from seismic imagery (inverse calibration) was built on the following analytical steps.

Firstly, detailed and extensive petrophysical analyses of outcrop (plug) samples, continuous core and sonic well logs, in combination with a quantification of mineralogical and textural properties, allowed a direct conversion of acoustic properties (impedance) into sedimentological properties, resulting in a quantitative physical sequence stratigraphic model.

Secondly, the integration of scale-dependent acoustic measurements, ranging from 0.01 m and 320 kHz on cores up to the wavelength of field seismic data was established using an averaging algorithm (an effective-medium-theory type) as an upscaling approach. This alternative to a VSP or check shot allows an optimized depth–time conversion and hence determination of the origin of the seismic reflections with previously unattainable accuracy.

Finally, the shape and scale dependence of impedance contrasts were integrated into so-called singularity parameters that directly link depositional changes with information from seismic reflections: depositional changes in the shallow-water domain are generally characterized by step functions, whereas those in more distal depositional environments are represented by spiky functions. This approach allows the recognition of the associated reflection events and, vice versa, it provides a unique opportunity to extract the character of impedance changes, and thus changes in depositional environment, from seismic reflection records in general.

*E-mail: hendrik.braaksma@dstu.univ-montp2.fr

This integrated and multiscale characterization of sharp-based shoreface deposits calibrates the typical reflection patterns for such sedimentary units. These include continuous high-amplitude smooth and flat tops, discontinuous sharp basal reflections with variable amplitude, and complex sigmoidal high-amplitude reflections within the compound shoreface deposits. In addition, the results of this study, by detailing the effects of scale and frequency on impedance changes, improve the identification of similar deposits in subsurface seismic data and the extraction of maximum amounts of geological information beyond seismic resolution.

INTRODUCTION

Today, most of the known hydrocarbon reservoirs in the world are located in structural traps. This is understandable since subsurface structure often has pronounced vertical expression, making these traps relatively easy targets to find. With most of the structures already drilled, attention in the last few years has turned increasingly towards stratigraphic traps (Ziolkowski, Underhill and Johnston 1998).

At conventional seismic scales, stratigraphic traps rarely have the vertical expression that would allow them to be clearly defined by conventional seismic techniques and display, and no consistent diagnostic criteria exist to define them. Since there is growing realization that the seismic signal itself is not the ultimate detection tool, the identification, classification and exploration of stratigraphic traps require an interactive, integrated and multidisciplinary approach that focuses geological, petrophysical and geophysical expertise on the same geological object. We have tackled this in a so-called 'natural observatory'.

The observatory, and topic of this paper, is located in the Boulonnais, along the English Channel coast in northern France, and consists of an Upper Jurassic succession (Oxfordian-Tithonian) of offshore marine shales and minor lime-mudstones interbedded with sharp-based shoreface deposits (Proust *et al*. 1993, 1995; Herbin *et al*. 1995; Wignall *et al*. 1996). Sharp-based shoreface deposits are major components of epicontinental basin fills. They are exclusively formed in low-gradient depositional settings under forced regression and can prograde over relatively long distances (Posamentier *et al*. 1992). Because stratal relationships are so subtle, because physical contrasts generally are strata-bound and because sharp-based shoreface deposits generally are not very thick, geological recordings of these sea-level falls and potential reservoirs are easily overlooked or unseen in seismic sequence stratigraphic analyses. The interval studied crops out in fresh cliff faces and is available under fully saturated conditions for surface seismic imaging, marine seismic imaging, subsurface drilling, coring and logging only a few hundreds of metres away (Fig. 1).

The unique character of the observatory allowed us to obtain very high detail and accuracy: the outcrop was geometrically quantified and was sampled for acoustic properties, grain-size and carbonate content, and a 3D surface seismic survey was conducted on the adjacent beach (Fig. 1). A variety of wireline logging tools were deployed in boreholes within and close to the seismic cube. The resulting data set comprises acoustic and geological parameters at overlapping scales and frequencies (Fig. 2). The following analytical approach was built on three important and discrete steps that form the basic structure of this paper.

The first step focuses on the translation of geological parameters into geophysical and petrophysical properties. This follows earlier work on seismic outcrop modelling (Rudolph, Schlager and Biddle 1989; Biddle *et al*. 1992; Stafleu and Schlager 1993; Helland-Hansen, Helle and Sunde 1994; Bracco Gartner and Schlager 1999; Kenter *et al*. 2001) and establishes a quantification of the relationship between sedimentological and acoustic properties and vice versa. In order to establish a relationship in time and space, the depositional environment across a complete depositional ramp profile (cf. Ahr 1973; Read 1985; Burchette and Wright 1992) was physically quantified. Combining the quantified depositional environment and its evolution through time with a physical characterization of systems tracts and their key bounding surfaces allowed us to construct a quantitative sequence stratigraphic model of the ramp margin on which the Upper Jurassic succession was deposited (Braaksma *et al*. 2006). By populating this model with acoustic properties acquired at a cm-scale, the geological parameters were translated into geophysical parameters, transforming qualitative sequence stratigraphy into a quantitative physical sequence stratigraphic model.

The second step ties seismic recordings in the time domain with geological and petrophysical observations in the depth

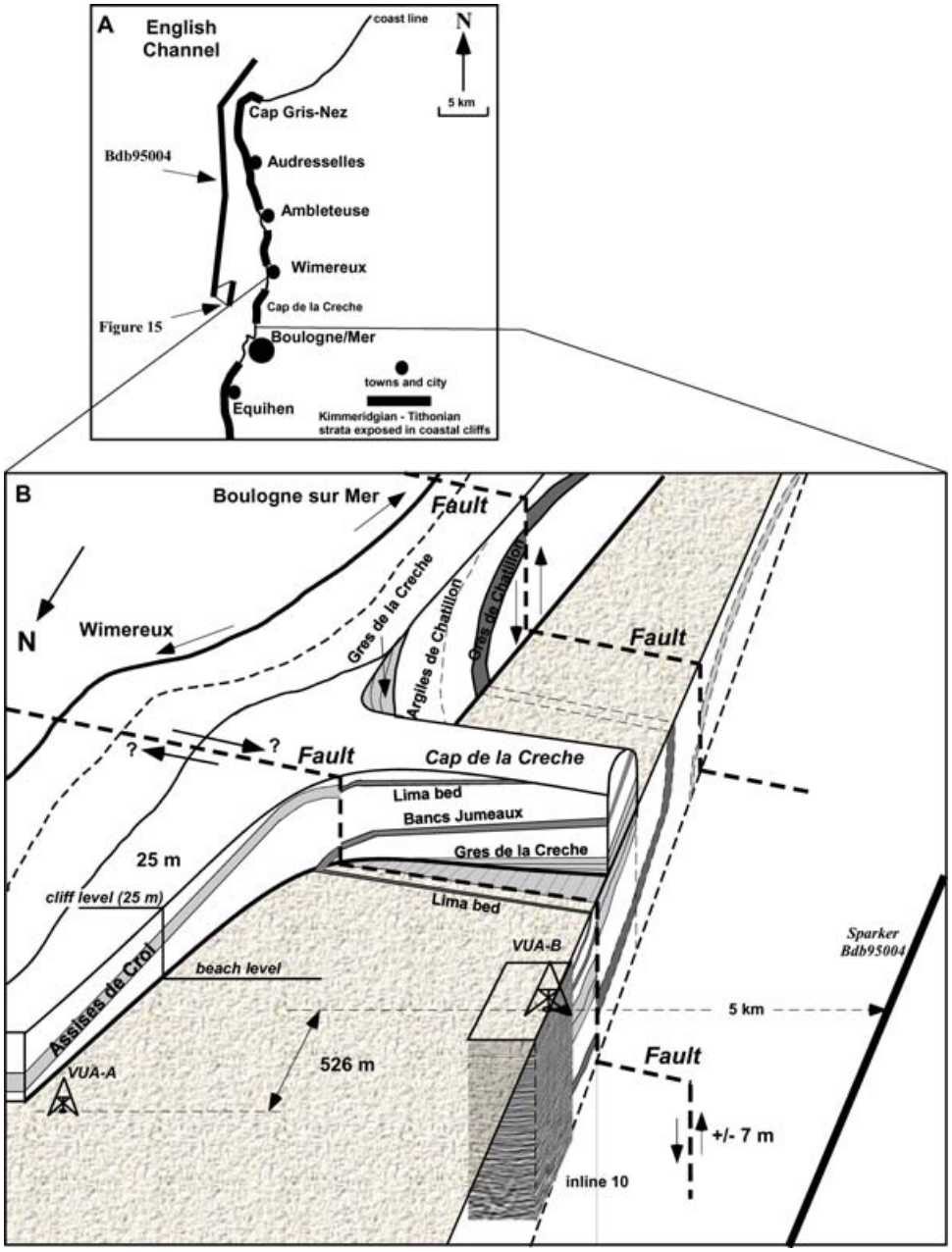

Figure 1 The Boulonnais observatory. (A) Location of the observatory; the location of the seismic line of Figure 15 is indicated. (B) Bird's-eye view of the Boulonnais observatory along the English Channel coast in north-western France viewed from the NNW. Between the town of Wimereux and the city of Boulogne-sur-Mer, Upper Jurassic strata are folded into a monoclinal structure. At the beach level, a 3D seismic survey was performed (square) and borehole VUA-B was drilled. A second borehole (VUA-A) was drilled a year earlier and is located directly south of Wimereux.

domain. An unconventional effective-medium-theory type of moving averaging algorithm is the underlying philosophy in this approach, and provides a well-to-seismic tie with previously (conventionally) unattainable accuracy. As a result, the origin of seismic reflection events can be determined and geological reasons for these events can be inferred. Although check shots and/or VSPs are normally used and preferred for time-depth conversion, this upscaling approach is a good alternative when these seismic techniques are absent or not trustworthy.

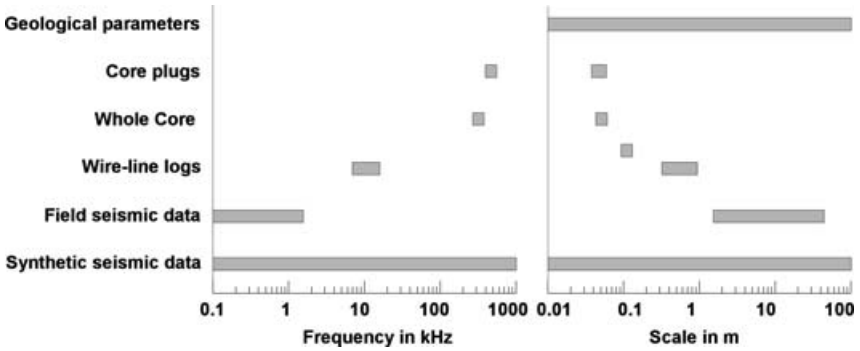

Figure 2 Overview of the frequency and scale of acquired geological and geophysical parameters in the natural observatory in the Boulonnais.

The third step comprises a multiscale analysis of impedance functions. This modulus maxima analysis yields two important parameters for the extraction of geological information from seismic images. First, a natural hierarchy in impedance events is established that can directly be related to incident frequency-dependent seismic reflectivity. Second, by parametrization of the shape (step versus spike functions) and scale dependence of impedance contrasts, a direct quantitative relationship between depositional changes and information from seismic reflections can be established. This integrated approach allows the recognition of scale-dependent reflection events and, vice versa, it provides a unique opportunity to extract the character of impedance changes, and thus changes in depositional environment, from seismic reflection records in general.

Finally, the discussion section reviews the results and factors that control the origin, nature and scale dependence of seismic reflections of sharp-based shoreface deposits. This analysis provides the means to extract maximum geological information from seismic images of these kinds of deposits that may have potential as subtle stratigraphic traps (e.g. Posamentier *et al*. 1992; Posamentier and Chamberlain 1993).

REGIONAL SETTING AND OUTLINE OF THE OBSERVATORY

In the Late Jurassic period of north-west Europe, a thick and economically significant source-rock accumulated in shallow epicontinental seas. The Wessex-Weald Basin is the southernmost of a series of basins stretching from southern England to the northernmost North Sea (Oschmann 1988), and the Boulonnais region is situated near the eastern termination of this basin close to the London-Brabant High (Wignall *et al*. 1996). This basin lacked a clear shelf-slope break and was characterized by extremely low angle slopes over large areas (Wignall 1989; Proust *et al*. 1995; Hallam 1997), which favoured the development of sharp-based shoreface deposits over accretionary shorefaces (Proust, Mahieux and Tessier 2001). In the Strait of Dover, the mixed siliciclastic-carbonate Kimmeridge Clay Formation is confined to five horizons of offshore marine shale, interbedded with sharp-based shoreface sandstone bodies (Herbin *et al*. 1995; Proust *et al*. 2001). A high-resolution sequence stratigraphic analysis of the Boulonnais succession could be correlated with more distal parts of the Wessex-Weald Basin (Williams *et al*. 2001; Taylor and Sellwood 2002; Braaksma *et al*. 2006) and major parts of the Paris Basin (Proust *et al*. 1995; Guillocheau *et al*. 2000) through unconformities and equivalent chronostratigraphic units.

The Upper Jurassic stratigraphic section studied is preserved in continuous steep cliff outcrops just below and just above the mean sea-level in the Strait of Dover, in the north-west of France. This provides a unique opportunity to set up terrestrial and marine reflection seismic experiments over the same interval to obtain high-resolution seismic reflection images and, more importantly, to have the ability to calibrate these imaging techniques with the true geological picture, as exposed in the adjacent outcrops (Fig. 1B). To aid in this ground-truthing of seismic reflection imagery, two boreholes (VUA-A and VUA-B) were drilled (Fig. 3A) and fully cored (Figs 3B.C.D). In the boreholes, various wireline logging tools were deployed to capture nearly all possible petrophysical and geological parameters at different and sometimes overlapping scales (Fig. 2).

DATA

Geological parameters and acoustic properties

A total of 1187 samples were selected for the analysis of grain-size and carbonate content. 440 samples with an average spacing of 30 cm were collected from the outcrop. 218 and 529 samples were selected from the cores of boreholes VUA-A and VUA-B, respectively, where for the latter an average spacing

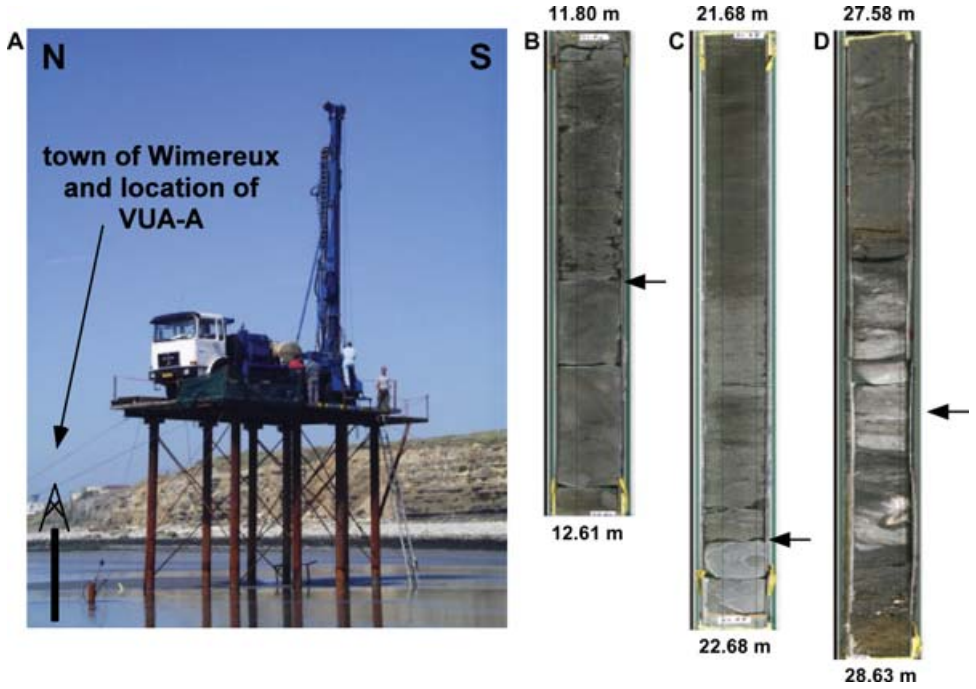

Figure 3 (A) Borehole VUA-B on the beach south of Wimereux, set in the intertidal zone. Since the tidal difference in the Boulonnais area can reach over 9 m, a platform was built in the centre of the seismic cube. The cliff outcrop visible in the background consists of flat-lying continuous Tithonian strata of the Assises de Croï Formation (overlying the Argiles de Wimereux Formation). On the far left, the location of borehole VUA-A is indicated. (B) True RGB-colour digital scan of high-quality core from borehole VUA-B. The arrow indicates the sharp boundary (P2 sequence boundary) of the uppermost tight limestone bed of the Bancs Jumeaux and the Argiles de Wimereux Formation. (C) Digital colour scan of the transition of the Grès de la Crèche Formation and the Argiles de la Crèche Formation (arrow). (D) Digital color scan of the basal part of the Marnes Intercalaire Formation. Note that the cemented sandstone beds form whitened bleached zones. The lateral continuity of these 'whitecaps' is directly controlled by the lateral extent of the overlying lignite-rich argillaceous, generally uncemented sand layer.

of 25 cm was achieved. Procedures used in the determination of acoustic properties of discrete 1 and 1.5 inch samples from borehole cores and outcrop have been extensively described by Braaksma *et al*. (2003).

Monopole sonic P-wave velocities used in this paper were determined in borehole VUA-B using a full-waveform sonic tool (2SAA-1000/F Full Waveform Sonic: MountSopris Instruments Co. Inc.) with a centre frequency of 15 kHz. This tool was equipped with four receivers (spaced at intervals of 1 ft) and logging was done under open-hole (no casing), fully saturated conditions. Waveform picking was performed manually to ensure good-quality data.

Density was measured using a formation gamma-density tool (EGS, Luxembourg), and natural gamma radiation was measured using a spectral gamma-ray tool (ANTARIS, MEDUSA, TNO-NITG). All wireline logging data were acquired with a sampling interval of 0.1 m.

A nearly continuous core of borehole VUA-B (recovery 93%) was analysed for V_P (centre frequency 320 kHz), gamma density, magnetic susceptibility and porosity (from gamma density, through grain-densities derived from the discrete samples from the same core), using a multisensor core logger (MST) with a sampling interval of 0.01 m. The full control of the geometry of the succession in the natural observatory (Fig. 1) allowed (small) gaps in core recovery to be filled in with outcrop-derived acoustic properties. In addition to physical properties, full colour RGB images of split cores were acquired (Figs 3B.C.D).

Field seismic data

For the acquisition of the seismic reflection data, a high-frequency hand-held (approximately 80 kg) P-wave vibrator was chosen. This specific source has the ability to generate acoustic sweeps from a few Hz to 1500 Hz, while allowing good control over the outgoing signal. High-frequency geophones with a natural frequency of 50 Hz were deployed and the recording system consisted of three networked seismographs.

The acquisition design was optimized using 144 channels to achieve a minimum fold of 24 and amplitude variations of less than 5% in order to minimize the acquisition footprint (Volker *et al.* 2000). Using a shot spacing of 3 m, a receiver spacing of 1.5 m, a template of two parallel 72-channel receiver lines, shooting and moving five templates to acquire one swath and repeating this five times, the coverage for this acquisition design is 36 fold. For the processing, Promax 3D was used. All processing steps used were standard (for industry-type seismic), with the exception of a prestack dip-moveout processing followed by a poststack time migration.

METHODS

Step 1: Quantitative relationship between acoustic properties and depositional environment

For quantitative characterization of the key surfaces and systems tracts of the Late Jurassic ramp deposits in the Boulonnais, cross-plots of mean grain-size and sorting (the standard deviation around the mean) were used to characterize shoreface composition generically, through a continuum of possible sedimentological parameters and/or lithofacies. Their position within the stratigraphic record was also examined in this context (Braaksma *et al.* 2006). In order to make use of the entire sample population in the grain-size analysis of every individual sample, all statistics were calculated using the logarithmic method of moments (Blott and Pye 2001). By populating the granulometric facies distribution in the sorting-mean space with acoustic properties, the standard qualitative sequence stratigraphic analysis of the succession (e.g. Wignall 1991; Proust *et al.* 1993, 1995, 2001; Herbin *et al.* 1995; Tribovillard *et al.* 2001) can be converted into a quantitative physical sequence stratigraphic model. This model bridges the gap between geological observations and geophysical determinations.

Step 2: Scale effects on velocity dispersion: the key to an optimized well-to-seismic tie

Small-scale layering and heterogeneity affect wave propagation (Marion, Mukerji and Mavko 1994) and therefore the seismic image. Theoretical (Helbig 1984), numerical (Carcione, Kosloff and Behle 1991; Marion *et al.* 1994) and experimental (Melia and Carlson 1984; Marion *et al.* 1994) results indicate that when the wavelength is much larger than the layer spacing ($\lambda \gg d$, or $\lambda/d \gg 1$), layered media behave as homogeneous (transversely anisotropic) media, where effective-medium theory (EMT) is applicable (Levin 1979; Mavko, Mukerji and Dvorkin 1998).

In ray theory (RT) or short-wavelength limits ($\lambda \ll d$, or $\lambda/d \ll 1$), the effective P-wave velocity for waves travelling normally to the layering of a stratified medium is given by the harmonic average (Marion *et al.* 1994). In the short-wavelength limit (RT), multiples arrive as separate events, whereas in the long-wavelength limit (EMT), the primary wave interferes with small-scale multiples, and this can lead to a delay in the arrival of the wave (Verhelst 2000). This effect of short-period multiple scattering on the phase velocity is referred to as a stratigraphic filter (O'Doherty and Anstey 1971; Kennett 1974; Banik *et al.* 1985a,b; Shapiro and Zien 1993).

The transition where RT behaviour changes into EMT behaviour also depends on the impedance ratio of the layers. For a synthetic stationary (periodically layered) case, where high-impedance layers represent tight-cemented sandstones or argillaceous limestones, and where the low-impedance layers represent claystones or uncemented sandstones (resulting in an impedance ratio of around 3.06), the transition from short- to long-wavelength behaviour occurs around a λ/d-value of 5 (Fig. 4A). This transition appears to be slightly dependent on incident frequency: with higher frequencies the transition zone widens from a λ/d-value of 5 in both λ/d-directions (Fig. 4A).

When modelling stacks of plastic and steel (impedance contrast ratio of 14.53; Fig. 4B), the abrupt transition, calculated with the wavefield-propagation-and-reflection (WRW) model (Berkhout 1982, 1984; Berkhout and Wapenaar 1990a,b), compares very well with the experimental transition range of λ/d between 10 and 15, but less well with the numerical transition around 7 of Marion *et al.* (1994).

Because sedimentary rocks generally are non-periodically layered, the wave propagation cannot be described by one single λ/d-value. Transmission experiments on randomly stacked layers show that increments of propagation time follow RT closely in zones with thick layers, and they follow EMT in zones of thin layers. The transition between RT and EMT occurs in these experiments at around the same λ/d-value as in stationary ones (Rio *et al.* 1996).

To calculate the propagation time normal to layering correctly, a composite method is applied. This method (after Verhelst 2000; originating from Sams and Williamson (1994) and Rio *et al.* (1996)) consists of two steps:

1 windowed effective-medium theory (EMT),
2 ray theory (RT).

The first step regularizes the small-scale variability in such a way that RT may be applied. In a medium with only fine-scale variability, the running average in the first step will yield

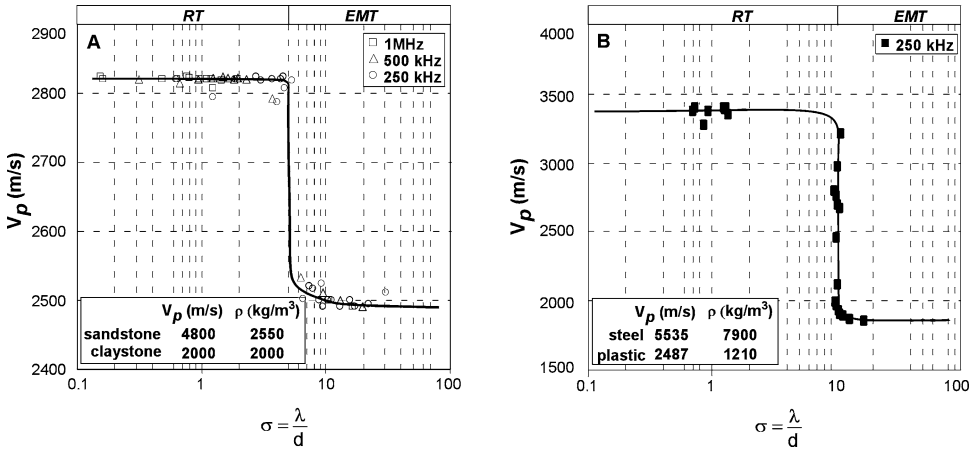

Figure 4 Numerical transmission experiments at the transition from short-wavelength behaviour (RT) to long-wavelength behaviour (EMT). (A) Cross-plot of numerically derived V_P as a function of the ratio of wavelength (λ) to layer spacing (d) for realistic impedance values for sedimentary rocks. Calculations for 1 MHz, 500 kHz and 250 kHz are indicated by squares, triangles and circles, respectively. The transition occurs at $\sigma = 5$. (B) The same experiment but for a synthetic case of steel and plastic layers.

a slowly varying effective medium. If this fine-scale variability is fairly stationary, this may even be treated as a constant effective medium. This first step differs from the continuous wavelet transform (Mallat 1999) only in the smoothing function: the Gaussian smoothing function used in this step is not a wavelet (Verhelst 2000). With only long-scale variability, RT is dominant and the first step of the composite method will have little effect.

By defining the scale of interest (e.g. seismic wavelength, receiver spacing of a sonic tool), the scale σ_z at which the medium needs to be averaged using EMT is defined as

$$\sigma_z = \frac{scale}{5}, \tag{1}$$

where the factor 5 is derived from the previous transmission experiments as illustrated in Fig. 4A. The P-wave velocity, smoothed to scale σ_z, is subsequently calculated back from EMT averaging results (basically a smoothing of compressibility) by applying an inverse calculation to correct for smoothed density and smoothed compressibility (Verhelst 2000).

The regularization or upscaling approach is applied to the MST P-wave velocity log (V_P MST). The effect of the regularization of V_P MST is a smoothing of the original log (Fig. 5A) with increasing scale σ_z. In Fig. 5(B), only two regularized velocity curves are plotted, whereas in Fig. 5(C), 120 of these curves are plotted next to each other, and the value of the regularized V_P is plotted vertically (coming out of the paper) in greyscale. This 'look-up table' for V_P for a range of scales, is a result of the upscaling of the original V_P MST to a scale σ_z of 2.56 (Fig. 5C). This range corresponds, in the case of a well-to-seismic tie, with wavelengths ranging from 0.05 to 12.80 m, recalling that the ratio of the scale at which a medium needs to be observed (scale) and the scaling operator (σ_z) equals 5.

However, in a seismic reflection survey, the seismic wave is measured in time instead of depth. The link between the wavelength in time (λ_t) and in depth (λ_z) is the scale-dependent velocity, and solving this link is a typical 'catch-22 problem' (Herrmann 1997; Verhelst 2000): the regularized velocity being the link between the wavelength in time and the wavelength in depth is dependent on the scale itself. Following Verhelst (2000), the 'catch-22 problem' is handled using an iterative procedure that finds the exact combination of the wavelength in time (λ_t) and the scale-dependent velocity in depth. This procedure starts by taking an initial constant scale in depth. For the ith iteration, the scale is updated using the velocity evaluated at the scale obtained from the (i–1)th iteration where the depth-to-time conversion is updated at every iteration step as well. After a certain number of iterations, the combination of the non-stationary scale operator, $\sigma_z^{(n)}$ in depth and the regularized velocity, $V_P(\sigma_z^{(n)}(z))$ in depth, match the desired wavelength, λ_t/d in time, exactly. Thus a perfect tie between well logs and seismic reflection data is achieved.

Step 3: Multiscale characterization of acoustic data

Continuous wavelet transformation is used in applications where the time-variance of the Fourier spectrum is of interest, as in time–frequency analysis and localized time-domain

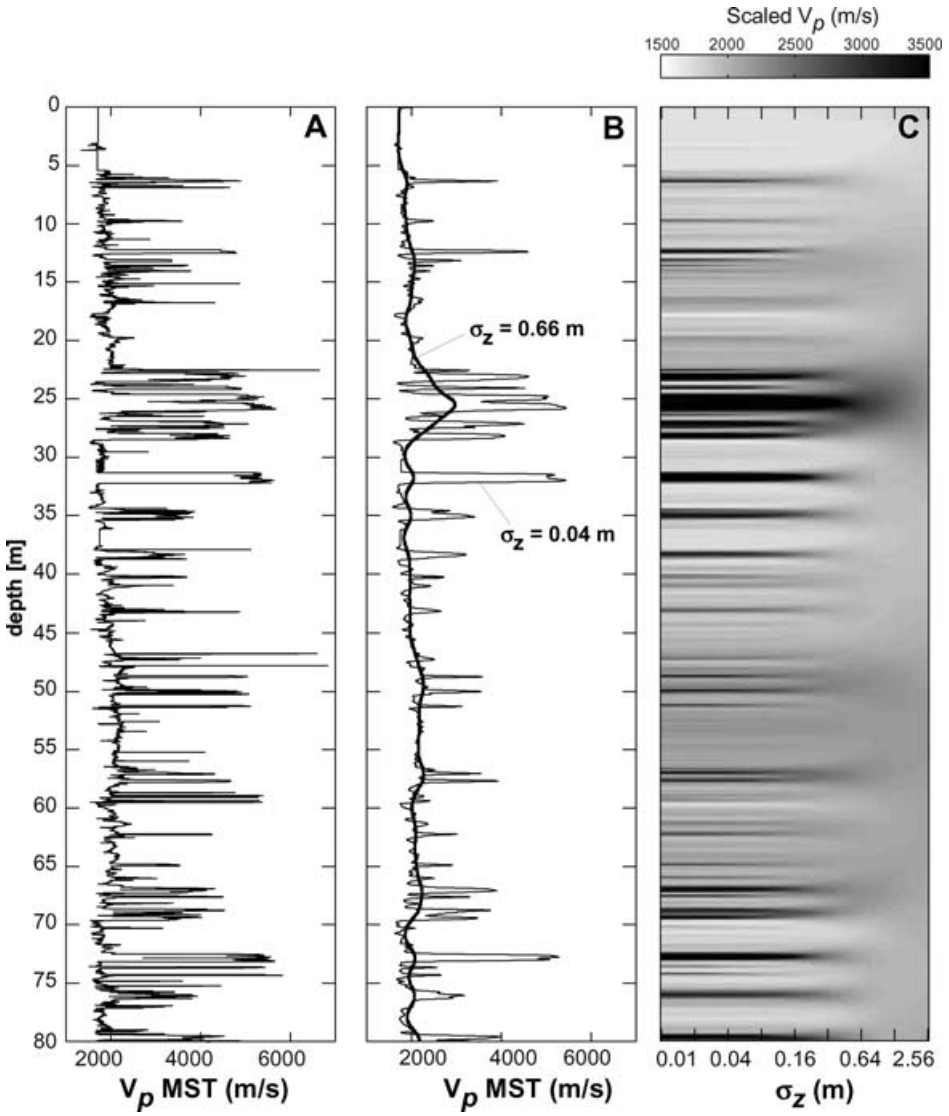

Figure 5 The composite upscaling method to account for the non-stationarity of layered media. (A) The original V_P MST log of borehole VUA-B cores with $dz = 0.01$ m (B) Results for the regularization of the P-wave velocity of V_p MST and using density MST. With increasing scale σ_z variations in the original V_P MST are smoothed and mean effective velocities decrease. (C) Regularized velocities and their scale dependences. This figure shows the upscaled velocity using running effective-medium averaging for a scale range $\sigma_z = [0.01$ m, 2.56 m]. This corresponds (using $\lambda_z/\sigma_z = 5$) to wavelengths of approximately $\lambda_z = [0.05$ m, 12.80 m].

filtering (Goudswaard 2001). The power of this wavelet transformation lies in its combined localized and zooming behaviour within signals, by making use of a 'mother wavelet' (the function for analysing any signal). It was developed to provide a means of reconstructing original functions from their representations or transforms in the form of seismic reflection data (Goupillaud, Grossmann and Morlet 1984). Wavelet transform analysis is a powerful tool for identifying and characterizing sharp perturbations in signals, where it will have its largest amplitudes (Goudswaard 2001).

The continuous wavelet transform is used in many applications (e.g. noise reduction and edge detection) and is used here for performing modulus maxima analysis. The purpose of the latter is to extract local singularity exponents that characterize singularities or irregular structures in signals (arrows in Fig. 6A), such as, for example, wireline logs (Grossmann and Morlet 1984; Mallat and Hwang 1992; Herrmann 1997).

In modulus maxima analysis, a local extremum in a signal is defined as any point where the first derivative of the signal has

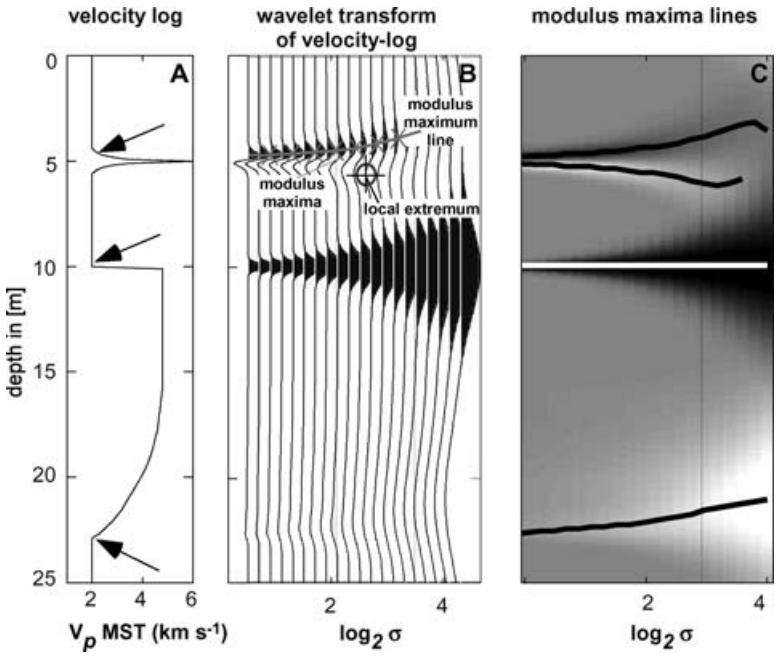

Figure 6 Modulus maxima analysis. (A) A velocity log with three isolated singular points, where the middle is described by a step function. (B) Wavelet transform of (A), for a discrete set of scale values. Definitions used in modulus maxima analyses are indicated. (C) Position of modulus maxima lines in the wavelet transform in (B).

a zero crossing (in the circle in Fig. 6B). In continuous wavelet transform analysis, a range of scales (σ_z) is analysed and the modulus maximum is defined as any point in the scale–depth space where local extrema occur (crosses in Fig. 6B). Modulus maxima lines are defined as curves connecting modulus maxima points (the grey line in Fig. 6B). These lines now characterize singularities in the velocity log in depth, for scale. This characterization is more generally applicable to the characterization of fractals.

Fractals have two intrinsic properties, scale-invariance and self-similarity. Scale-invariance means that an object looks the same at all scales and self-similarity means that any part of a (natural) system, appropriately enlarged, looks like the whole (Anstey and O'Doherty 2002; Purkis 2004). In his classic paper, Mandelbrot (1974) defined fractals as functions which obey a local scaling symmetry. In fractals, the parameter α is called the singularity exponent (also referred to as a Hölder exponent), and it characterizes the singularity strength of a particular singular point. If the wavelet transform of an impedance contrast (for example, let us take a tight limestone bed embedded in shale; Fig. 3B) remains symmetric over a range of α-values, it is called multifractal (Goudswaard 2001). A singularity with a singularity exponent α has a cone-like structure in the σ_z-direction (with increasing scale) of the wavelet transform, originating from the position of this singularity in the log used (Figs 6B.C). This is quite similar in appearance as the upscaled velocity shown in Fig. 5(C).

RESULTS

Step 1: Quantitative relationship between acoustic properties and depositional environment

Measured sedimentological and acoustic properties from the first 80 m of borehole VUA-B are shown in Fig. 7. Figure 7(A) shows the grain-size distribution. The colour code indicates the frequency of relative abundance of siliciclastic material in predefined grain-size classes (56 in total). The relative abundance increases from deep blue to deep red. Clear coarsening-up (interpreted as shoaling) events can be observed as well as major breaks in shoaling trends. The boundaries for clay (< 8 μm), silt (> 8 μm and < 63 μm) and sand (> 63 μm) are indicated by the dashed lines. Figure 7(B) shows the calcium carbonate content, measured on the same samples that were used to determine the grain-size distribution. These two logs together quantitatively describe the solid media on which various acoustic measurements were performed.

The acoustic velocity V_P was measured at different scales (dz): on the nearly continuous core with $dz = 0.01$ m (Fig. 7C), in the borehole with $dz = 1$ ft (RX2, Fig. 7E), with $dz = 2$ ft (RX3, Fig. 7F) and with $dz = 3$ ft (RX4, Fig. 7G). As can be observed from these logs, with coarser scales of acoustic measurements, the absolute value of V_P decreases and jumps in V_P are smoother.

Natural gamma radiation is generally regarded as a good lithology indicator. Spectral measurements of gamma radiation can provide even more insights into the lithology over

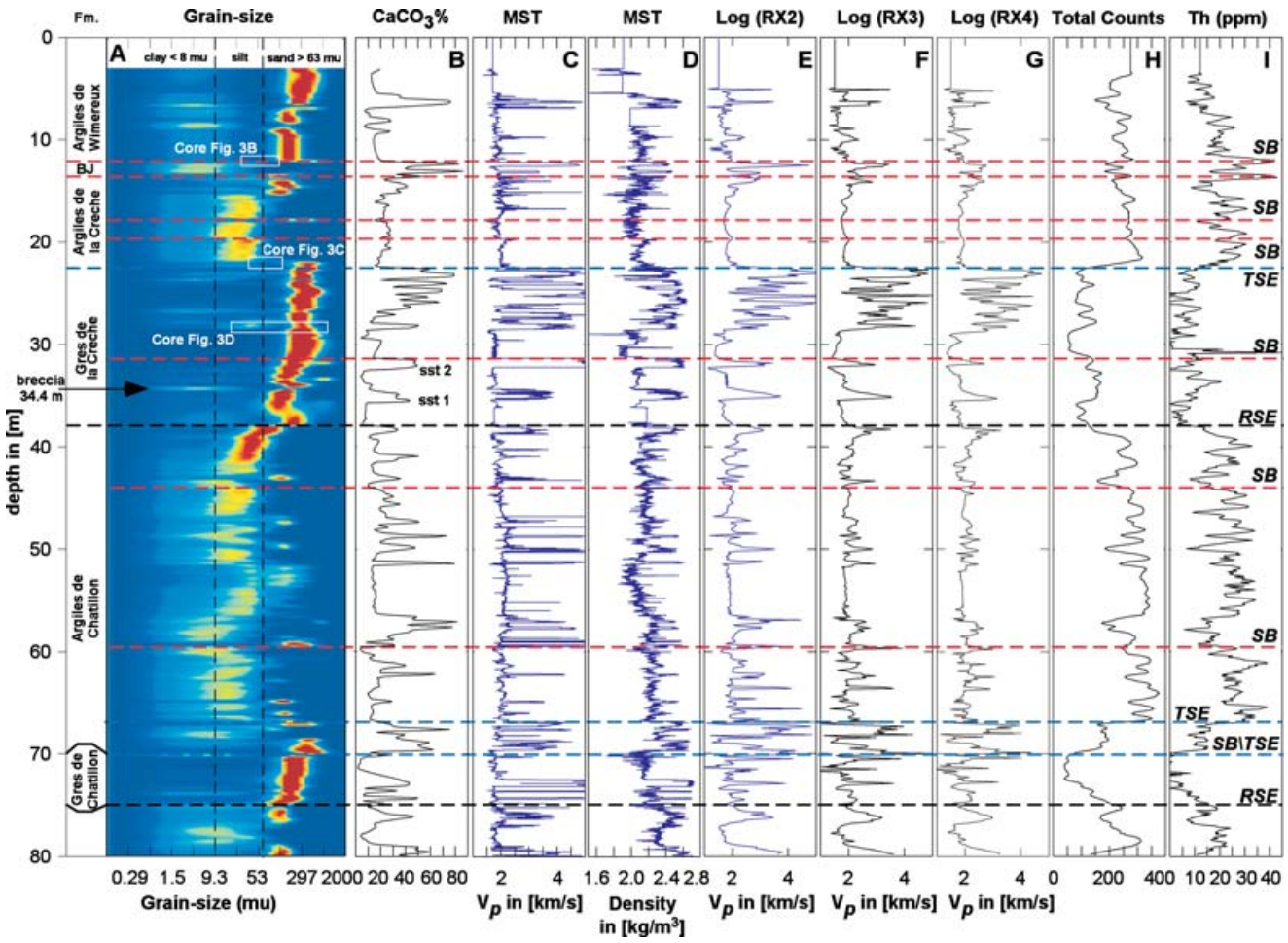

Figure 7 A selection of measured sedimentological and acoustic properties from the VUA-B core and well for the first 80 m (A) Grain-size distribution; the colour-code indicates the frequency of relative abundance of siliciclastic material in predefined grain-size classes (56 in total): the relative abundance increases from deep blue to deep red. Coarsening-upward events (interpreted as shoaling events) can be observed as well as major breaks in shoaling trends. The boundaries for clay (< 8 μm), silt (> 8 μm and < 63 μm) and sand (> 63 μm) are indicated by the dashed lines. (B) Bulk calcium carbonate content measured on the same samples that were analysed for grain size. (C) V_P measured on the core, using the MST with $dz = 0.01$ m, with a centre frequency of 320 kHz. (D) Gamma density measured on the core using the MST with $dz = 0.01$ m (E) Sonic (wireline) log, measured with a centre frequency of 15 kHz over an interval $dz = 1$ ft (0.3048 m). (F) Sonic log, centre frequency 15 kHz over an interval $dz = 2$ ft. (G) Sonic log, centre frequency 15 kHz over an interval $dz = 3$ ft. (H) Gamma ray in total counts. (I) Spectral gamma ray: the thorium contribution to the total counts of natural gamma radiation and sequence stratigraphic surfaces (see text for discussion).

which the measurement was performed, by segregating the total counts (Fig. 7H) into the three most abundant naturally occurring radionuclids K, U and Th (Fig. 7I). As expected, most sandy units and limestone beds are characterized by low gamma-ray values. However, spectral gamma-rays cannot differentiate well between carbonate-rich and carbonate-poor sandstone units (Fig. 7).

Based on grain-size trends in three sections within the observatory (VUA-A, VUA-B and the outcrop at Cap de la Crèche, Fig. 1), a sequence stratigraphic interpretation of the Late Jurassic succession was performed (Braaksma *et al*. 2006). The most important (sequence) stratigraphic surfaces are indicated in Fig. 7.

The integration of 18 240 measurements of acoustic properties (acquired at different scales) and 1187 measurements of textural and geochemical properties is shown in Fig. 8. In the density–velocity space (Fig. 8A), the various data sets all follow the same trend (increasing density with increasing P-wave velocity and vice versa), but they show that MST, outcrop and core-plug samples have higher velocity values than those from the wireline logs, although density values of all data sets are comparable. The trends of these data sets do not follow

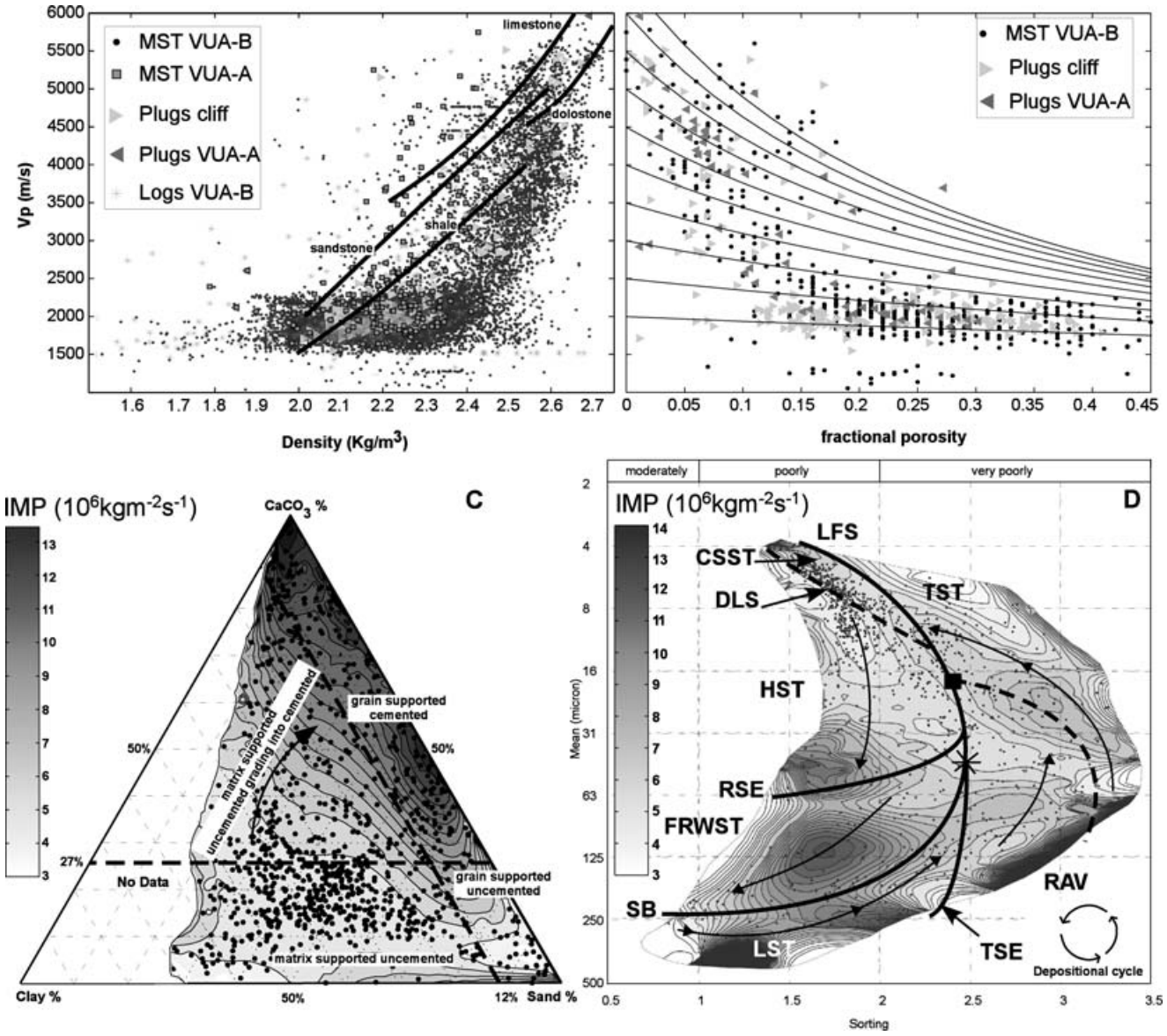

Figure 8 Integration of all acoustic, mineralogical and textural measurements acquired at different scales. (A) Cross-plot of density and V_P for various scale and frequency-dependent data sets. The various empirical equations of Gardner *et al*. (1974) cut the Boulonnais data set at a steeper angle (see text for discussion). (B) Cross-plot of porosity and V_P for a selection of the complete data set. This figure shows that the time-average equation for various matrix velocities (Wyllie *et al*. 1956) cannot adequately explain the observed trends in the high-velocity range. (C) Ternary plot of the main constituents of the solid matrix, calcium carbonate, clay and sand (including silt-sized particles). Contours in the ternary diagram indicate impedance; the black dots mark the position of each individual sample (1187 in total). (D) Cross-plot of mean grain-size and sorting (standard deviation around the mean grain-size). Contours indicate impedance. This figure illustrates the physical quantification of depositional environments, systems tracts and their key bounding surfaces.

the popular velocity transform of Gardner, Gardner and Gregory (1974) very well. This discrepancy can be explained by the fact that most of Gardner's experimental transforms originate from deeper buried rock formations, whereas the maximum overburden of the stratigraphy in the Boulonnais area did not exceed 500 m before uplift and erosion (El Albani *et al*. 1993). The large continuous data groupings and the broad range of V_P and density values show that this case study captures nearly all the variability in the acoustic properties of sedimentary rocks in general (Carmichael 1990). Comparing

a smaller part of the data set against another popular velocity transform shows that the time-average equation for various matrix velocities (Wyllie, Gregory and Gardner 1956) cannot adequately explain the observed trends in the high-velocity range. They do, however, follow the low-velocity variation between porosity and velocity (Fig. 8B).

Porosity (and density) exerts primary control on acoustic velocity and impedance. Mineralogy, grain-size and texture control the remainder of the variation (Braaksma *et al*. 2003). By decomposing the bulk rock sample into its main constituents, i.e. $CaCO_3$, clay and sand (including silt-sized particles), not only can the variation in impedance (besides porosity) be quantitatively assessed, but also a direct link between acoustic properties and depositional environment can be made (Fig. 8C). Although no clear thresholds can be defined, a general trend is that clay and carbonate content have opposite and overlapping effects on acoustic impedance: the influence of clay content progressively increases with decreasing carbonate content (Braaksma *et al*. 2003). Significant changes in impedance do overlap, in part, with traditional classification boundaries such as, for example, the change from grain- to matrix-supported aggregates (Vernik and Nur 1992) as indicated in Fig. 8C.

The multivariate statistical analysis of granulometric facies and bulk carbonate content provides a physical quantification of depositional environments, systems tracts and their key bounding surfaces across a depositional profile (Braaksma *et al*. 2006). This analysis provides important insights into the lateral continuity of petrophysical and geochemical parameters above and below bounding surfaces, it can be used to assess qualitatively the diagenetic mechanisms controlling the formation of carbonate cements, and it can elucidate the distribution of acoustic properties within sharp-based shoreface deposits and their overlying and adjacent strata. The bounding surfaces were mapped on to Fig. 8D using the following procedure: grain-size measurements from every sequence that, where possible, was interpreted at the three section locations (boreholes VUA-A and VUA-B and the outcrop, see Fig. 1 for locations) were plotted in the sorting–mean space. The key bounding surfaces, separating the different coded systems tracts are the same as those indicated with thick black lines in Fig. 8(D). Using the different sharp-based shoreface deposits (e.g. Grès de Châtillon and Grès de la Crèche) as (bathymetric) tie points and assuming Walther's law, a spatial characterization of the systems tracts from their more proximal (Grès de la Crèche) location to their most distal (Calcaires de Brecquerecques, not shown here but located below the Grès de Châtillon) location, with respect to the palaeo-shoreline, was constructed (Braaksma *et al*. 2006). The most important features that can be observed in Fig. 8(D) can be summarized for a full depositional cycle as follows:

The sequence boundary (SB) separates the forced regressive wedge systems tract (FRWST) from the lowstand systems tract (LST) and has limited lateral extent, because it merges basinwards with the transgressive surface of marine erosion (TSE) and a local flooding surface (LFS). Following the SB from left to right, i.e. going from proximal to more distal depositional settings, i.e. with ongoing sea-level rise, and comparing impedance values on both sides of the SB trajectory, it is clear that the SB is characterized by a discontinuous impedance-contrast distribution, resulting in a non-uniform distribution of reflectivity values (positive, zero and negative) along the SB trajectory from proximal to distal depositional settings.

When preserved, the overlying LST is characterized by a large range of impedance values. Most proximally and at the lowest point on the sea-level curve, low impedance values dominate (bottommost left area). With a sea-level rise, or at more distal locations on a slope profile, indicated by increasing sorting values (becoming less well sorted), LST sandstones can become cemented by calcium carbonate, yielding higher impedance values. Extremely high weight-percentages of $CaCO_3$ (up to 70%) suggest that bioclastic material and minor relatively coarse-grained sands must have dominated the initial composition before pronounced diagenesis. At the most distal location, impedance values are intermediate to low.

The transgressive systems tract (TST) occupies the largest area in the sorting–mean space (area to the right of the TSE-LFS). The dashed line indicates the approximate position of a transgressive ravinement surface (RAV), separating the early (or proximal) TST from the late (or distal) TST. The TST as a whole is fining-upwards, first with increasing sorting values (becoming less well sorted) in the early TST, and then decreasing sorting values (becoming better sorted) in the late TST. Only very poorly sorted sediment at the base of the RAV and in the middle of the TST show elevated impedance values.

The maximum flooding surface (MFS), located within the condensed section systems tract (CSST), which is bounded by the LFS at its base and the downlap surface (DLS) at its top, records an impedance contrast only in most distal depositional environments (upper left corner of Fig. 8D).

The highstand systems tract (HST) is characterized by lowest impedance values. A gradual increase can be observed when coarsening-upwards (shoaling). In proximal to

intermediate depositional settings, the top part of the generalized HST is characterized by intermediate to high impedance values. In intermediate to distal depositional settings, i.e. following the trajectory of the RSE from left to right in Fig. 8(D), impedance values decrease rapidly and in most distal depositional settings no impedance contrast between the generalized HST and the overlying FRWST is observed.

In more proximal depositional locations (better sorted), the regressive surface of marine erosion (RSE) marks a dramatic jump in impedance values, resulting in positive reflectivity values. Basinwards (becoming less well sorted), this jump is less well-defined and at most distal depositional settings, no impedance contrast is associated with this surface.

The forced regressive wedge systems tract (FRWST), like the LST, is characterized by a large range of impedance values and occupies a significant area in the sorting–mean space (Fig. 8D). Within the overall uncemented sands of FRWST, the carbonate-cemented sandstone bed at 34.5 m (sst 1 in Fig. 7) has an erosional coarse-to-very-coarse, glauconite-enriched base, contains synsedimentary faults in the middle of the bed and shows a coarsening-upward trend in grain-size (Fig. 7A). The upper part of this bed consists of cm-scale sharp-based thick-thin mud/sand couplets, exhibiting oscillation ripples, and is formed under an oscillatory flow regime followed by relatively short periods of relative quietness when fines could settle from suspension. This bed is interpreted as having formed in a lower shoreface/transition zone of a fair-weather, wave-dominated shoreline (facies 4 of Wignall *et al*. 1996) and is sharply overlain by a phosphate and lignite (wood) containing, clay-rich breccia layer (34.4 m in Fig. 7A). This association of sedimentological features indicates deposition on an inclined surface. It may therefore represent the front of a migrating sequence, which has been truncated by a transgressive surface of marine erosion during a high-frequency sea-level oscillation, superimposed on an overall sea-level fall. The sharply overlying breccia layer and a marked increase in total gamma-ray counts at this level (Figs 7H.I) indicate the reworking of parts of this clinoform during relative sea-level rise.

The actual impedance contrast of the sequence boundary originates from an interval of uncemented, relatively coarse-grained argillaceous sands with cm-sized quartzite pebbles at the base and a highly cemented, 92 cm thick sandstone bed below (sst 2 in Fig. 7). The latter has a sharp erosional base, contains synsedimentary faults in the upper part of the bed, exhibits a coarsening-upward trend in grain-size (Fig. 7A), shows swash cross-stratification and is interpreted as having formed in a foreshore setting. The upper bed within the FRWST (just below the SB) is interpreted as the front of a migrating more steeply inclined sequence (clinoform). This is based on sedimentological similarities between the two high-impedance beds, on the strata-bound carbonate cementation (Fig. 7C) and on the similar sorting and mean grain-size characteristics of the high-impedance sandstones in the generalized FRWST (Fig. 8D). However, the dissimilarity in sedimentary structures (thick-thin mud/sand couplets exhibiting oscillation ripples versus swash cross-stratification) between the two carbonate cemented beds indicates an overall lowering of relative sea-level during the deposition of the FRWST of the Grès de la Crèche Formation. Furthermore, the interval overlying the upper high-impedance bed (sst 2) is characterized by an extreme jump towards high thorium values (Fig. 7I), whereas the total gamma-ray counts are decreasing (Fig. 7H). These opposite trends may suggest exposure and soil development associated with this unconformity (Ogg 1995). This sequence boundary can thus be classified as a Type–1 sequence boundary (cf. Van Wagoner *et al*. 1988; Schlager 2004). On the other hand, such a marked opposite jump in the two gamma-ray logs is not observed (both logs show a gradual increase) for the interval overlying the lower high-impedance bed. Therefore, exposure is not inferred.

The basal bed of the FRWST directly overlies the RSE unconformity. This bed has not been subjected to profound cementation and therefore it is characterized by (initial) low impedance values over the entire ramp profile (Fig. 8D)

Step 2: Scale effects on velocity dispersion: the key to an optimized well-to-seismic tie

For an exact well-to-seismic tie, the non-stationary scale operator, $\sigma_z^{(n)}$ in depth and the regularized velocity, V_P $(\sigma_z^{(n)}(z))$ in depth have to match the desired wavelength, $\lambda_t/5$ in time, exactly. For the extraction of the time-varying dominant wavelength λ_t from the seismic data, image analysis was performed on synthetic and real seismic sections.

Using the WRW model to calculate full-waveform reflection seismograms over a frequency range from 765 to 15 Hz, a 'look-up table' is created for the frequency content contained within broadband seismic-reflection images and signals (Figs 9B.C). This table not only illustrates the effect of the incident wavelets used and the reflection resolution achieved, but also shows that seismic picks of geological boundaries are not unique and are a function of incident seismic frequency,

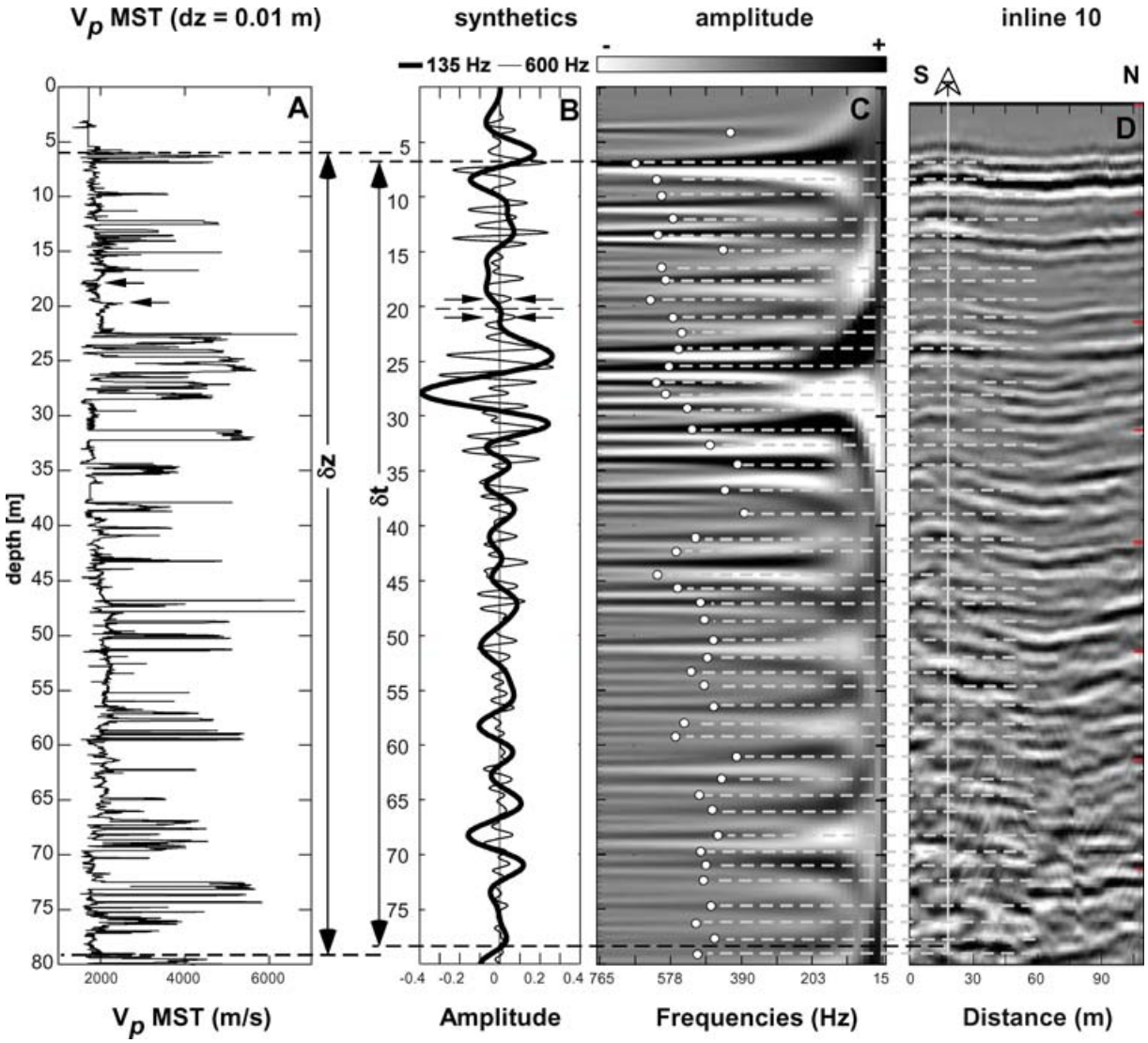

Figure 9 Dominant wavelength extraction from the seismic reflection data. (A) Original VUA-B V_P MST with $dz = 0.01$ m (B) Two synthetic seismic traces for 135 and 600 Hz. (C) 51 synthetic seismic traces at various frequencies plotted next to each other; the amplitude is plotted in grey scale. Plotted on top this 'look-up table' for frequency content are the best matching positions of frequency with respect to the reflections observed in the seismic image of (D) (see text for discussion). (D) Zero-phase reflection seismic image shot on the beach between Wimereux and Boulogne-sur-Mer, where the position of borehole VUA-B is indicated by the white line.

also referred to as tuning phenomena (Sengbush, Lawrence and McDonald 1961; Widess 1973). The latter can be quantified by instantaneous phase analysis (Taner, Koehler and Sheriff 1979). For example, the two positive velocity contrasts at 17.80 and 20.0 m (arrows in Fig. 9A) can be identified as separate reflection events until a frequency of approximately 333 Hz. With lower frequencies, these two events merge into one single reflection event, whose maximum amplitude pick lies in between the picks for each individual event (Figs 9B.C).

By correlating panels C and D in Fig. 9 visually, and by taking into account the length and the strength (phase and amplitude, respectively) on and around each synthetic and real reflection event, an approximation of the dominant wavelength in time is extracted from the real seismic image (the white dots in Fig. 9C) at the location of borehole VUA-B (white line Fig. 9D). Other, more robust mathematical methods like the matching pursuit method (Mallat and Zang 1993) are available and in essence do the same as the matching approach followed here.

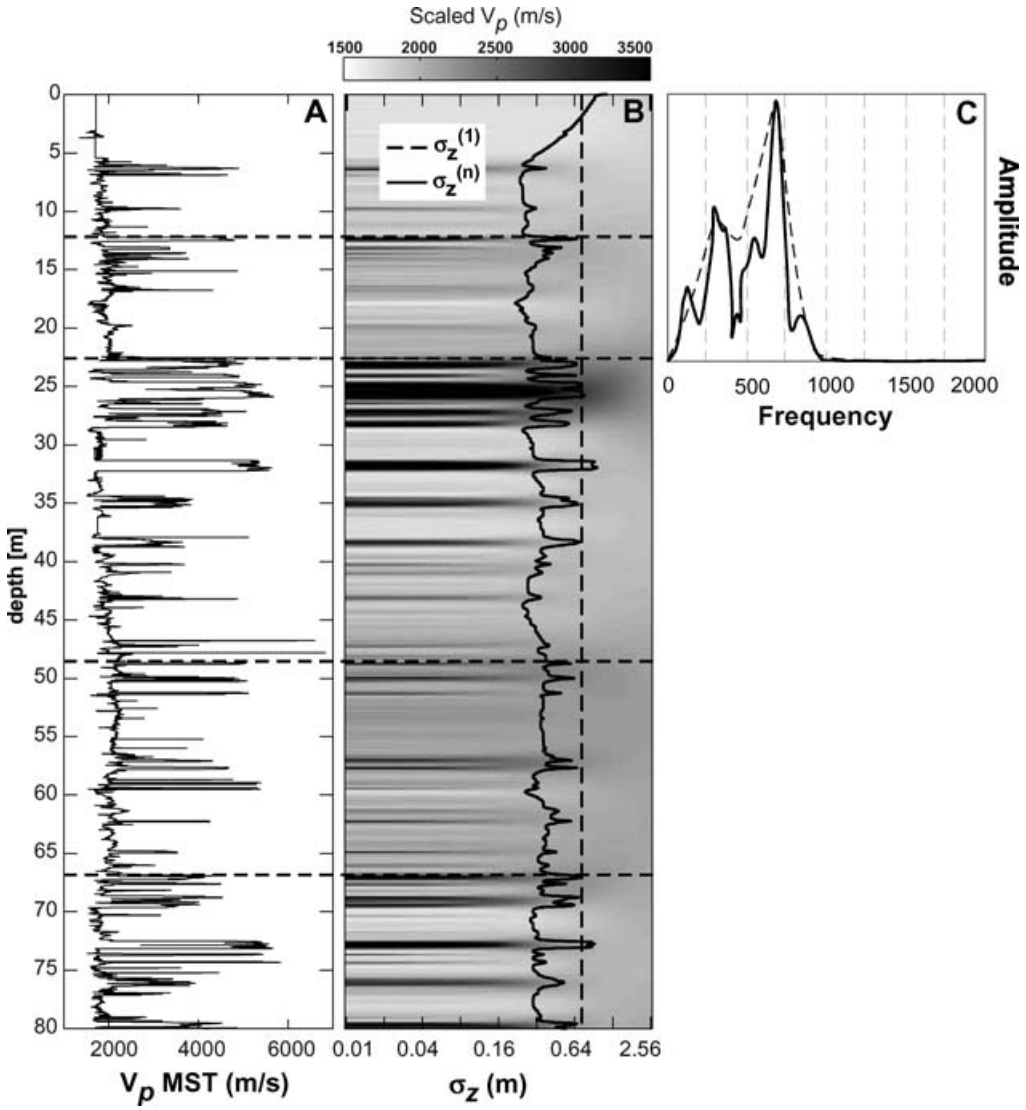

Figure 10 Iteration results for borehole VUA-B, to match exactly the combination of the non-stationary scale operator, $\sigma_z^{(n)}$ in depth and the regularized velocity, $V_P(\sigma_z^{(n)}(z))$ in depth with the desired wavelength, $\lambda_t/5$ in time. (A) Original V_P MST. (B) As Figure 6(C), where the dashed line was used as the starting point of the iteration and the full black line shows the regularized velocity log of the final iteration. (C) Frequency content extracted from the seismic image at the position of VUA-B using the TracePAK module in Kingdom suite.

To handle the 'catch 22-problem', a constant scale $\sigma_z = 0.73$ was used, as indicated in Fig. 10(B) by the dashed line. This value for σ_z is derived from

$$\frac{V_{P(RT)(mean)}}{5 \times frequency} = 0.73, \quad (2)$$

where the dominant non-localized centre frequency of the seismic image is around 625 Hz (Fig. 10C) and the mean RT-velocity of the original V_P MST log equals 2280 m/s. After 7 iterations, the combination of the non-stationary scale operator, $\sigma_z^{(n)}$ in depth and the regularized velocity, $V_P(\sigma_z^{(n)}(z))$ in depth exactly match the desired wavelength, $\lambda_t/5$ in time (Fig. 10B, solid black line).

Having measuring the effective P-wave velocity through the layered Upper Jurassic succession at five different scales, the composite regularization method can be tested for its applicability to the Boulonnais data set. Another way of showing the effect of regularization is to plot the mean regularized velocity over the analysed interval versus the scaling parameter (Fig. 11). The mean velocity of the original V_P MST log is

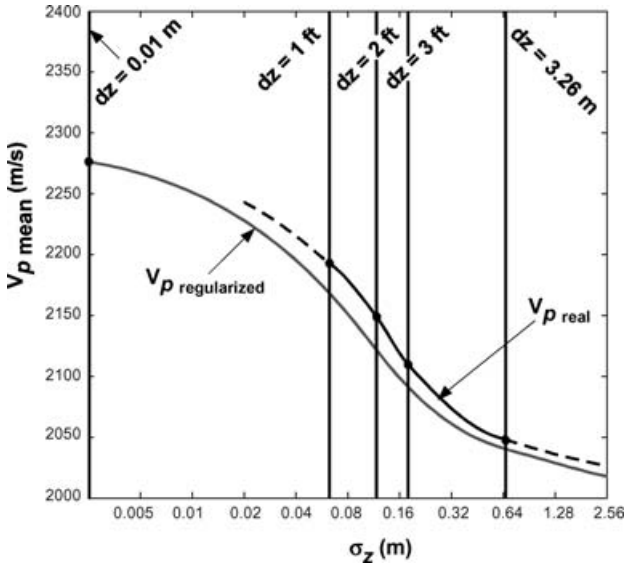

Figure 11 Integration of scale-dependent acoustic measurements. The mean regularized velocity is plotted in grey against the scaling parameter (σ_z). Black dots indicate the mean RT-velocities measured at different scales d_z for the three sonic logs and for the reflection seismic experiment. The relative error $((V_{\text{Preal}} - V_{\text{Pmodelled}})/V_{\text{Pmodelled}})$ is only 0.95%. See text for discussion.

plotted on the far left, and along the grey line, the mean velocity after regularization is clearly decreasing with increasing scale (σ_z).

If a direct comparison between absolute values of V_P from sonic (acquired with a 1 ft receiver spacing of the sonic tool) and the original V_P MST ($dz = 0.01$ m) is the objective, the original V_P MST log needs to be upscaled to approximately 0.06 m (0.3048/5). For 2 ft and 3 ft receiver spacings, these scales become 0.12 m and 0.18 m, respectively. The seismic scale is approximated by $\sigma_z^{(1)}$ and equals 0.73 m (see above). Since a nearly perfect control of the depth-to-time conversion is achieved by this method (see Discussion), impedance (and V_P) contrasts in depth can be directly correlated with seismic reflections in time. The mean velocity at the seismic scale can therefore be calculated from the ratio δz (the distance in metres between two velocity contrasts) and δt (the distance between the two corresponding reflections) as illustrated in Fig. 9.

As can be observed from Fig. 11, the fit between V_P measured at a defined scale (sonic logs and seismic) very closely follows the modelled mean velocities from the composite regularization method. The calculated mean relative error is only 0.95%, which may be explained by the small difference between *in-situ* wireline logging (and seismic reflection experiments) and core-line logging under ambient pressure, where it must be noted that in this upscaling approach, anisotropy (Thomson 1986) is not taken into account.

Step 3: Multiscale characterization of acoustic data

The impedance log of the MST (IMP MST) in Fig. 12(A) shows that the conventional view of a layered subsurface consisting only of step functions (Zoeppritz 1919) is a major simplification of real impedance contrasts: the transition of acoustic properties from one layer to another can be smooth or gradual, as well. Figure 12(B) shows the wavelet transform of this log over a scale range from 0.005 to 5.12 m. A number of modulus maxima lines, three of which are highlighted, are plotted over the wavelet transform (Fig. 12B). A decrease in amplitude (for example, black to dark grey), as well as a widening of the cone (in depth), with increasing scale, can be observed along each line. When plotting the amplitudes along each line versus scale, different slope angles are calculated in the log-log space for each of the three acoustic contrasts (Figs 12C.D.E). These slope angles correspond to the α-values described above. Although not constant over the entire scale range, the assumption that α is constant in a certain scale range is much less restrictive than assuming step–function interfaces ($\alpha = 0$ everywhere), as is usually done (Goudswaard 2001). The singularity exponent α thus describes the impedance function, meaning the shape of the impedance contrast with depth and scale. In Fig. 12(G), different impedance functions and their corresponding α-values are displayed over a range of −1–0.4. Spiky contrasts have strong(er) negative α-values (Figs 12D.E), whereas step functions have an α-value of 0. α is plotted in Fig. 12(F) for a selection of modulus maxima lines.

As can be seen in Fig. 12(B), not all modulus maxima lines are equal in length. At a coarse scale of $\sigma_z = 2.56$ m, only 5 events remain. In this way a natural hierarchy in impedance contrasts can be established (Vermeer and Alkemaade 1992). The impedance contrast event that is highest in the hierarchy is the transgressive surface of marine erosion at 22.56 m, marking the top of the Grès de la Crèche Formation (Fig. 7). This sharp boundary is characterized by a step-like impedance contrast, which is quantified by an α-value of −0.138 (Fig. 12C). However, this surface does not coincide with the strongest impedance-contrast event. Highest reflectivity values occur at the sst 1 bed in the FRWST at 34.5 m (Fig. 7), although this contrast is not the highest in the natural hierarchy (Fig. 12B).

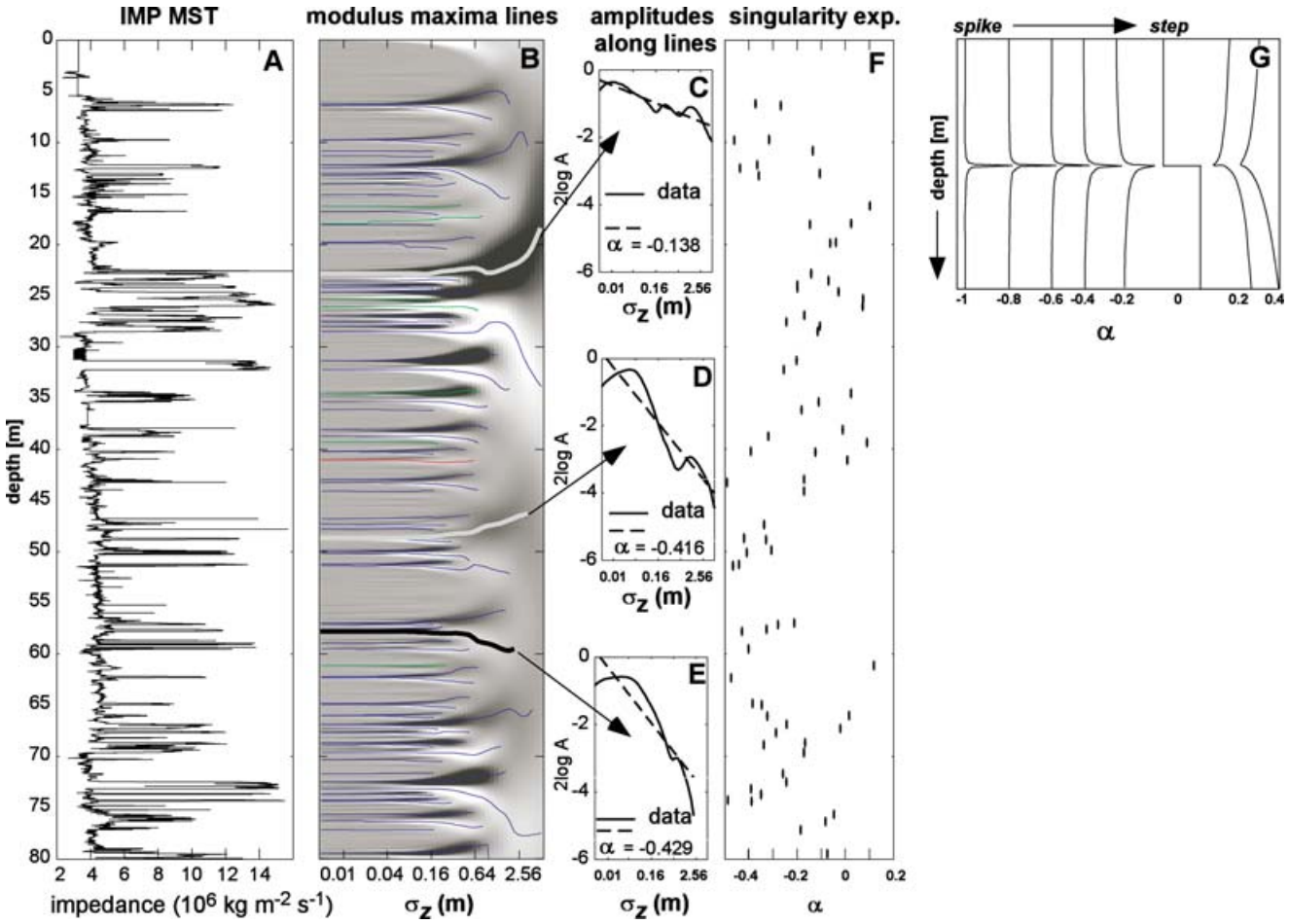

Figure 12 Multiscale characterization of VUA-B. (A) Original impedance log of the MST. (B) Modulus maxima analysis results, where modulus maxima lines are plotted over the wavelet-transformed IMP MST, displayed as a variable density plot in grey scale (see text for discussion). (C) (D) and (E) Double-logarithmic plots of the amplitudes along the highlighted modulus maxima lines in (B). (F) Singularity parameters (α, i.e. the slopes of linear regression results in the log-log space as displayed in (C) (D) and (E)) versus depth. (G): Impedance functions as a function of singularity parameter α, using a constant density and a velocity contrast ratio of 0.5 (after Goudswaard 2001).

DISCUSSION

Seismic impedance versus sedimentological information

Apart from incident frequency, seismic reflections are a function of impedance contrast and the shape of the impedance function. For the Boulonnais case, the impedance contrast at the physical contact between two contrasting layers is controlled by the interplay between initially deposited material (sediment flux) and, more importantly, the diagenetic overprint manifested by calcium carbonate cementation. Without this cementation, and thus framework stiffening, leading to an increase in the effective elastic moduli of an aggregate (Dvorkin and Nur 1998; Mavko *et al*. 1998), the impedance contrast between physically and lithologically completely different materials is not present (Fig. 8C). Impedance values (the product of density and V_P in Fig. 7) for uncemented sand units may even be lower than for shale units. The contour lines of equal impedance are, however, not parallel to gridlines of equal $CaCO_3$ content (horizontal lines in Fig. 8C), implying that sandy (coarser-grained) sediments are more susceptible to carbonate cementation than clayey (finer-grained) sediments. Since little to no porosity contrast is observed in carbonate-poor sediments (Braaksma *et al*. 2006), it is most likely that the initial permeability, in combination with the sedimentation rate (residence time on the seafloor in combination with wave-action and percolation) and the presence of carbonate

content as bioclastic material, controls the diagenetic process of cementation.

Sea-level fluctuation has a direct influence on acoustic impedance. At the positions on a slope profile where sea-level variations have the largest impact, which is typically in the proximal shallower parts of a sedimentary basin, carbonate cementation (leading to elevated impedance values) is most profound (Fig. 8D). In deeper depositional settings, concentrations of bioclastic material as storm-related shell-beds (Oschmann 1990; Wignall and Newton 2001) and hemipelagic carbonate deposition during times of extremely low clastic sedimentation, in combination with organic matter diagenesis (Berner 1980; Curtis 1987; Taylor *et al*. 2000), can lead to higher impedance values (Fig. 8D).

Well logs are just one-dimensional observations and, within a sedimentary system, acoustic properties can change rapidly in space. In the siliciclastics-dominated sedimentary system in the Boulonnais, vertical variations in acoustic properties are more pronounced than lateral variations, since the processes of cementation by $CaCO_3$ tend to follow subtle depositional bedding planes in the shallow part of the depositional environment, while storm-related shell-beds are usually laterally continuous in the intermediate environments, and hemipelagic carbonate mudstone beds lie in the deepest environments, following the initial flat seafloor morphology.

The outcrops around the seismic survey show a layer-cake stratigraphic succession and therefore no significant lateral variations in impedance contrasts are expected at the scale of the seismic experiment (Fig. 1). Seismic reflections are expected to be continuous and traceable over the full extent of the survey and the one-dimensional impedance characterization from the well is very likely to be representative of the entire stratigraphic volume that is seismically imaged.

However, to resolve impedance contrasts within the frequency ranges at which seismic experiments are generally performed (from 10 Hz up to 1500 Hz), they need to have a certain thickness. Furthermore, the type of impedance contrast (the impedance function) in the vertical sense (e.g. gradual or step-like) controls the amplitude and shape (phase) of the recorded seismic wavelet at those stratigraphically important positions (Verhelst 1998).

Heirarchy and nature of reflection events related to sea-level fluctuations

Impedance functions are scale-dependent and can be characterized numerically (Fig. 13). However, as already stated above, not all impedance events are strong enough to maintain amplitude over the entire scale range at which these events are analysed (Fig. 12B). The reason for this natural hierarchy of potential seismic reflectors is the shape of the impedance function, which is related to the 'thickness' and absolute value of the impedance of layers.

In addition to the V_P MST log, modulus maxima analyses were performed on all three sonic logs (RX2, RX3 and RX4). Density was not used in this analysis, and it is assumed that density does not change the characterization of singularity parameters fundamentally. At the scale these logs were acquired, as expected, the MST log yields the largest number of singularities, as this log was acquired with a sampling distance of 0.01 m. The sonic logs yield comparable numbers of singularities, all significantly lower than the MST log, whereas the seismic sections yield the lowest number (a maximum value since it is determined from the sum of all peaks and troughs) of singularities (Fig. 13A).

Since it is the seismic scale that is of interest, a selection of singularity parameters is made: only singularities that have modulus maximum lines longer than $\sigma_z = 0.16$ m (corresponding to seismic frequencies up to 700 Hz) are considered, although they originate from the singularity within the original log. Since the non-localized frequency content of the reflection seismic profile is around 625 Hz, the singularity parameter for any impedance event may be traced back to, or may be represented by, a reflection in the seismic reflection image.

Using this selection, the effect on impedance contrast classification by means of singularity parameter calculation is shown to be dependent on the scale at which the original log was acquired (Fig. 13B–E). Comparing the different scales, the wireline logs appear to be a little smoother than the MST log, and the MST log approaches zero α-values in the middle to top part more closely than the wireline logs. To assess the acquisition footprint quantitatively using singularity parameter classification, a linear regression between the α-values at a defined scale was performed. Figures 13(I.J.K) shows this regression for the three singularities highlighted in Fig. 13(F). From this, it can be inferred that α is dependent on the scale of acquisition, but that this dependence is complex. Since nearly all α-values are negative, positive slope values indicate a strengthening of α with increasing acquisition scale (from spike to step functions), whereas negative slope values imply weakening of α with increasing scale (from step to spike functions). Zero-slope values imply no scale dependence on acquisition, and are dominant where, in the original logs, the singularity is characterized by a step function (Fig. 13B–F).

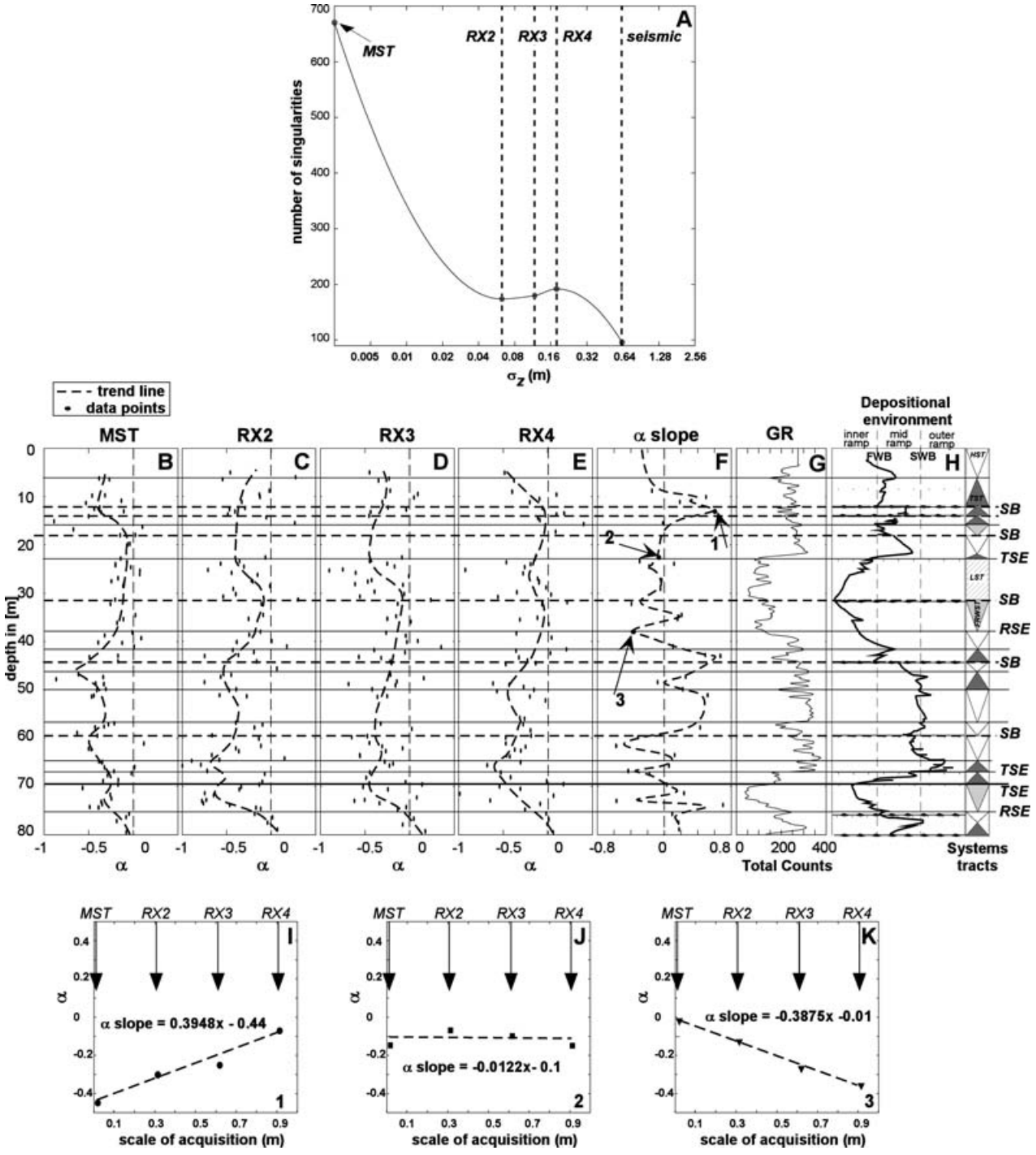

Figure 13 Hierarchy and nature of reflection events related to sea-level fluctuations. (A) Cross-plot of the number of singularities against the scale of acquisition of the acoustic data. With increasing measuring scale (*dz*), the number of singularities in the corresponding logs decreases (see text for discussion). (B) (C) (D) and (E) Modulus maxima analysis results on all acoustic logs (similar to Figure 11G). (F) Assessment of the acquisition footprint in α-classification (see text for discussion). (G) Gamma ray in total counts. (H) Reconstruction of depositional environment, where the black line indicates palaeo water depth. FWB = fair-weather-wave-base; SWB = storm-wave-base. On the far right, a simplified sequence stratigraphic interpretation is illustrated along with indications of major boundaries (HST = highstand systems tract; TST = transgressive systems tract; LST = lowstand systems tract; FRWST = forced regressive wedge systems tract; SB = sequence boundary; TSE = transgressive surface of marine erosion; RSE = regressive surface of marine erosion). (I) (J) and (K) Illustrations of the linear regressions of singularity parameters for defined scales, to assess the acquisition footprint on α-classification as displayed in (F).

A more important feature that can be observed in Fig. 13(B–E) is that all logs show a similar trend: from α-values of around zero at the base, to strong negative values around 50 m, and then a consistent increase in α-values until approximately 23 m. The top part shows a more inconsistent trend: from 13.50 m, the MST and the RX2 logs show an increase in α-values, whereas the other two wireline logs show decreasing α-values.

A comparison of the trend of α in depth with the gamma-ray log (Fig. 13G) and the reconstruction of depositional environments (Fig. 13H; Herbin *et al*. 1995; Mahieux *et al*. 1998; Proust *et al*. 2001; Braaksma *et al*. 2006) shows that major stratigraphic boundaries also mark changes in the characterization of impedance contrasts. Lowest α-values (spiky functions) are observed in the deepest-water environmental settings, whereas step-like functions are characteristic for shallow-water environmental settings.

In the hierarchy of impedance events, step functions are in the highest position. These events are most likely to be identified within the seismic frequency range (having amplitude in the modulus maxima space (σ_z–depth) within the seismic wavelength range (Fig. 12B)). Since these types of functions characteristically vary little in amplitude with increasing scale (α-values approaching zero), they may have the most consistent and most continuous seismic expression in terms of wavelet phase and reflection amplitude.

Singularity parameters for seismic reflections can be extracted from seismic data (Goudswaard 2001; Goudswaard and Wapenaar 2001). These authors show that the instantaneous phase of reflection events contains information complementary to the multiscale reflection amplitudes extracted from logs: this standard seismic attribute in seismic interpretation measures the phase shift of a specific reflection event and is generally used to check for consistency in the reflective behaviour of an impedance contrast (Taner *et al*. 1979; Goudswaard 2001). The nature of reflections in terms of instantaneous phase may therefore not only provide more information on the lateral consistency of impedance contrasts, but may also provide a direct link to other geological parameters, such as palaeodepositional environment, when a group of reflections (in a specific seismic time window) have characteristic α-values (Fig. 13).

However, in order to ground-truth the seismic reflection profiles recorded in time directly, to characterize their reflections in terms of singularity parametrization, and to correlate them with impedance contrasts through singularity parameter determination of wireline logs recorded in depth, a very accurate depth-to-time conversion is a prerequisite.

Well-to-surface-seismic ties through upscaled velocities

Tying wells to seismic is a crucial step in seismic reflection characterization, reservoir engineering (net and gross estimates) and seismic interpretation. A nearly perfect tie of well data and seismic data is established by upscaling acoustic well data to the wavelength of the reflection seismic profile, where it must be noted that this upscaling method is a fitting procedure. This implies that imperfections in the processed surface seismic image will still result in a good fit. The iterative upscaling procedure yields a localized velocity log in depth (Fig. 10B) that is used to convert the original log (V_P MST) into time (Fig. 14A), but also any other well log, e.g. the gamma-ray log (Fig. 14C). This allows a direct correlation between the seismic image (Fig. 14D) and geological parameters inferred from these logs or measured directly on cores and core samples.

Especially in the top and middle parts of the section, the expected layer-cake subsurface architecture is well reconstructed by the applied seismic imaging technique when taking the low-amplitude tectonic folding into account (Fig. 14D). Having established a nearly exact tie with well data (including cores) and obtained full knowledge of the depositional architecture from outcrop observations and core correlation, seismic reflections can be correlated directly with log signatures and tied to major stratigraphic surfaces (Fig. 14). Although the seismic image (Fig. 14D) does not show clear geometric relationships (except for the truncating flooding surface (fs) near the top of the Grès de la Crèche at 25.5 (ms), seismic sequence stratigraphy can be applied, based on outcrop studies and high-resolution grain-size sampling of outcrop and cores.

The relationship between sea-level cyclicity, impedance contrast classification and seismic reflectivity

A direct link exists between (sequence) stratigraphy and seismic signatures. To demonstrate this relationship, a trend line was fitted through α-values for different events, taking into account the fact that over major (para)sequence bounding surfaces, such as sequence boundaries and flooding surfaces, time hiatuses are present and possible dramatic changes in depositional environment may have occurred. For these reasons, the trend line is offset to higher negative α-values at certain places (Fig. 14B), recalling the fact that transgressive systems tracts are usually thin (Proust *et al*. 2001) and not all of them can be shown at this scale of observation (for a highly detailed sequence stratigraphic interpretation, see Braaksma *et al*. 2006).

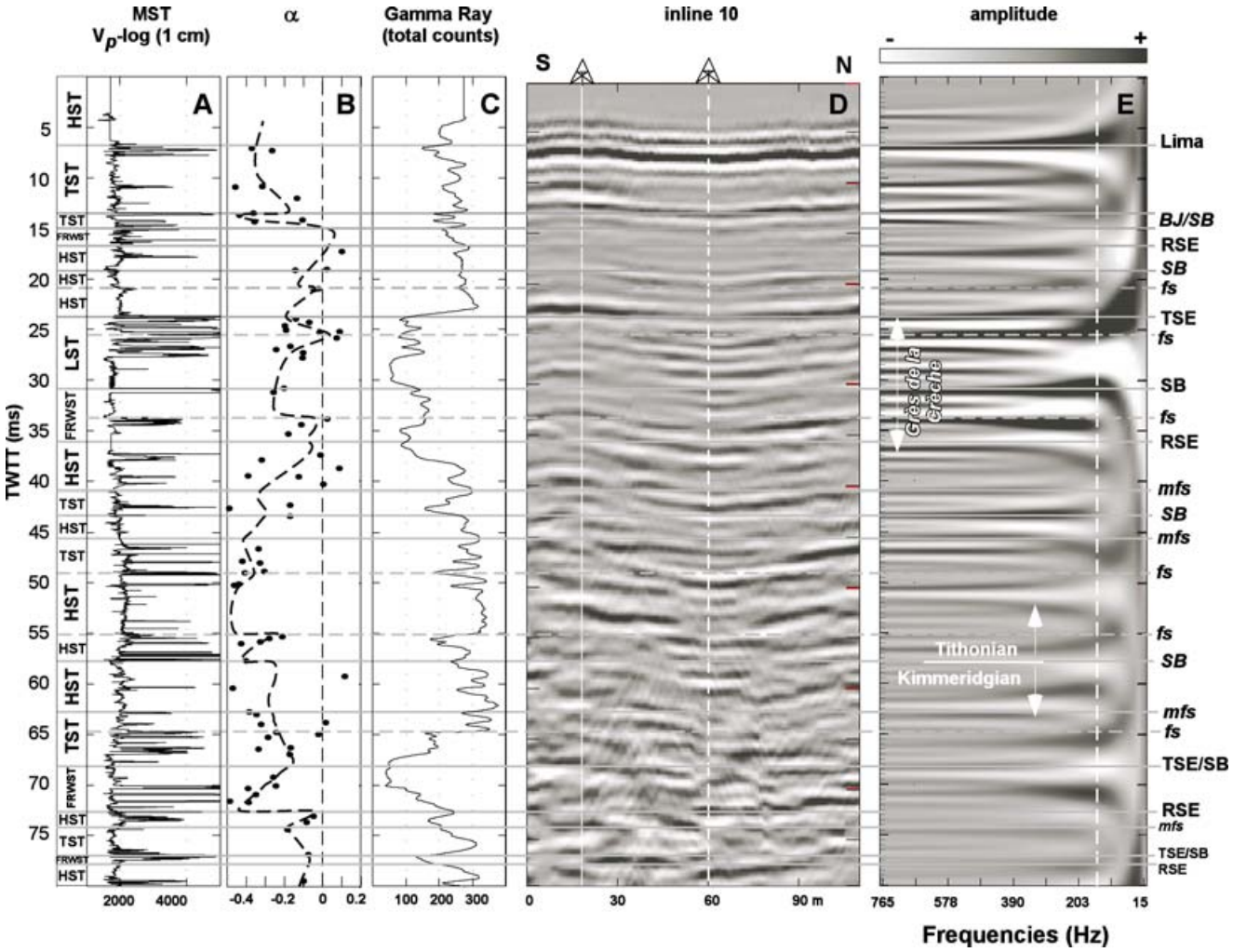

Figure 14 Well-to-seismic tie through upscaled velocities. (A) Sequence stratigraphic interpretation and the original V_P MST, now plotted in matching seismic time. (B) α-classification and trend line also plotted in time to allow a direct correlation with seismic reflection in (D) (see text for discussion). (C) Gamma ray plotted in time. (D) Reflection seismic imaging results, showing that this type of acquisition design can provide seismic images that show geological structure up to the intrinsic frequency of impedance layering (bedding rhythm). (E) Multifrequency synthetic seismic panel. See text for discussion.

In a sequence stratigraphic framework, the lowstand systems tract (LST) shows a gradual increase in α-values from the most proximal to more intermediate locations, where it is characterized by step-like impedance functions. Towards the topmost (or more distal) locations, a decrease can be observed (Fig. 14B). Seismic reflections are continuous and of high amplitude (Fig. 14D). The transgressive systems tract (TST) does not have characteristic α-values, but while deepening, a characteristic decrease towards more negative singularity parameters (spike functions) can be observed. Initial palaeobathymetry controls the starting point of this negative deviation. Seismic reflections are discontinuous and have highly variable amplitudes (Fig. 14D). The highstand systems tract (HST) is characterized by the largest variation in impedance functions (Fig. 14B). Although at some places quite tentative, a general increase in α-values towards more step-like impedance functions can be observed. Seismic reflections within this systems tract are either continuous with high amplitudes, or discontinuous with variable amplitudes (Fig. 14D). The forced regressive wedge systems tract (FRWST) also shows a large variation in α-values. For the Grès de Châtillon Formation, it is characterized by spike functions, whereas in the Grès de la Crèche, it shows a tendency towards step functions (Fig. 14B). For both, an increase in α-values towards step-like

impedance functions can be observed. Recalling that at the survey location the shoreface deposits of the Grès de Châtillon were deposited more distally than the shoreface deposits of the Grès de la Crèche (cf. Proust *et al*. 2001; Braaksma *et al*. 2006), the processes of carbonate cementation of the grains may not have been as intensive as for more proximally deposited sands. Therefore, thicker carbonate-cemented sandstone beds, resulting in step-function impedance characteristics are not formed, although absolute impedance values for these cemented beds may be similar to or even higher than cemented beds in the more proximally deposited shoreface (Figs 14A.B). Seismic reflections in the FRWST are continuous and of high amplitude for shallow depositional settings. However, at more distally located sections, these reflections change in character to more discontinuous reflections with highly variable amplitudes, resulting in a more chaotic reflection pattern (Fig. 14D).

Scale dependence of imaged sharp-based shoreface deposits

Having established a survey design that provided a seismic image displaying the geology nearly up to its intrinsic frequency of impedance layering (bedding rhythm), the effects of increasing scale (lower incident frequencies) on the seismic representation of the geologically (and physically) defined shoreface deposit can be addressed through the multifrequency synthetic seismic panel (Fig. 14E). Thus, this kind of panel can not only be used to extract the localized frequency content of seismic reflection images (Fig. 9), it can also provide insights into how sharp-based shoreface deposits may appear in seismic volumes acquired with more conventional, lower-frequency sources and/or when they are located deeper within the subsurface.

By decreasing the frequency, or by increasing the scale to 134 Hz (white dashed line in Fig. 14E), high-frequency reflection events lose their identity because of destructive tuning (Zeng and Kerans 2003) and show a decreased number of reflection events. The remaining reflections at this scale do not originate from one single impedance contrast, but are the net effect of multiple events. In terms of the hierarchy of reflection events, step-like impedance functions maintain their identity as a single event the longest. In the multiscale analysis of every impedance event in the MST log, these types of impedance contrast show the least amount of amplitude variation with increasing scale, whereas spike-like contrasts show the largest negative relationship in amplitude with increasing scale. However, when the scale dependence of a multiple-layer seismic response is examined (the multifrequency panel; Fig. 14E), it shows that although individually spike-like functions show a decrease in amplitude with increasing scale, multiple spikes together can merge into a reflection with clearly higher amplitudes. This constructive tuning phenomenon (cf. Sengbush *et al*. 1961; Widess 1973) seriously hampers the extraction of geological information from seismic images.

Although seismic reflection amplitudes become increasingly geologically conspicuous with lower frequencies, seismic images of composite sharp-based shoreface deposits do show a consistency in reflection pattern. They usually have a smooth top that dips seawards; they may show a complex middle part, depending on the thickness and preservation of a lowstand systems tract; and they have a basal part that cuts down into underlying highstand systems tracts. In this lower part, prograding concave-upwards clinoforms can usually be observed (Fig. 15; Tesson *et al*. 1990; Posamentier *et al*. 1992; Mahieux *et al*. 1998; Kolla *et al*. 2000; Posamentier and Morris 2000; Proust *et al*. 2001). Although acquired using terrestrial (instead of marine) seismic acquisition techniques and using a P-wave vibrator as a source, the composite sharp-based shoreface deposit of the Grès de la Crèche Formation shows a similar reflection pattern at intermediate-to-lower frequencies (Figs 14D.E):

It has a smooth top since, with shoreface retreat, subtle transgressive truncations of strata that are observed in outcrop are also resolved in seismic sections (Fig. 14: fs). The high-frequency complex middle part (LST) is less complex at lower frequencies, because no impedance contrasts are resolved at 134 Hz, and the three present at the highest frequencies (Fig. 14E) are constructively tuned into one at 450 Hz (Fig. 15).

The sequence boundary retains amplitude over the full frequency scale range (Fig. 14E) and is the only impedance event that, with increasing scale, does not lose its identity as a single impedance event. However, the relatively small distance between boreholes and cliff (Fig. 1) does not allow recognition of well-defined, high(er)-angle downlap patterns in the FRWST, which contrasts with the low-angle geometrical relationships of the underlying HST and the overlying LST, as observed in laterally more extensive marine seismic lines (Fig. 15). Because of the similarities between the two high-impedance sandstone beds within the FRWST, it is most likely that, at the scale of the observatory, the SB has truncated a more steeply inclined, highly cemented front side of a clinoform. This results in a step-like impedance contrast and a high-amplitude positive reflection over the entire frequency range. Thus, seismic imaging of the SB is directly related to the orientation of the seismic line with respect to direction of progradation and to the horizontal distance between successive clinoform truncations

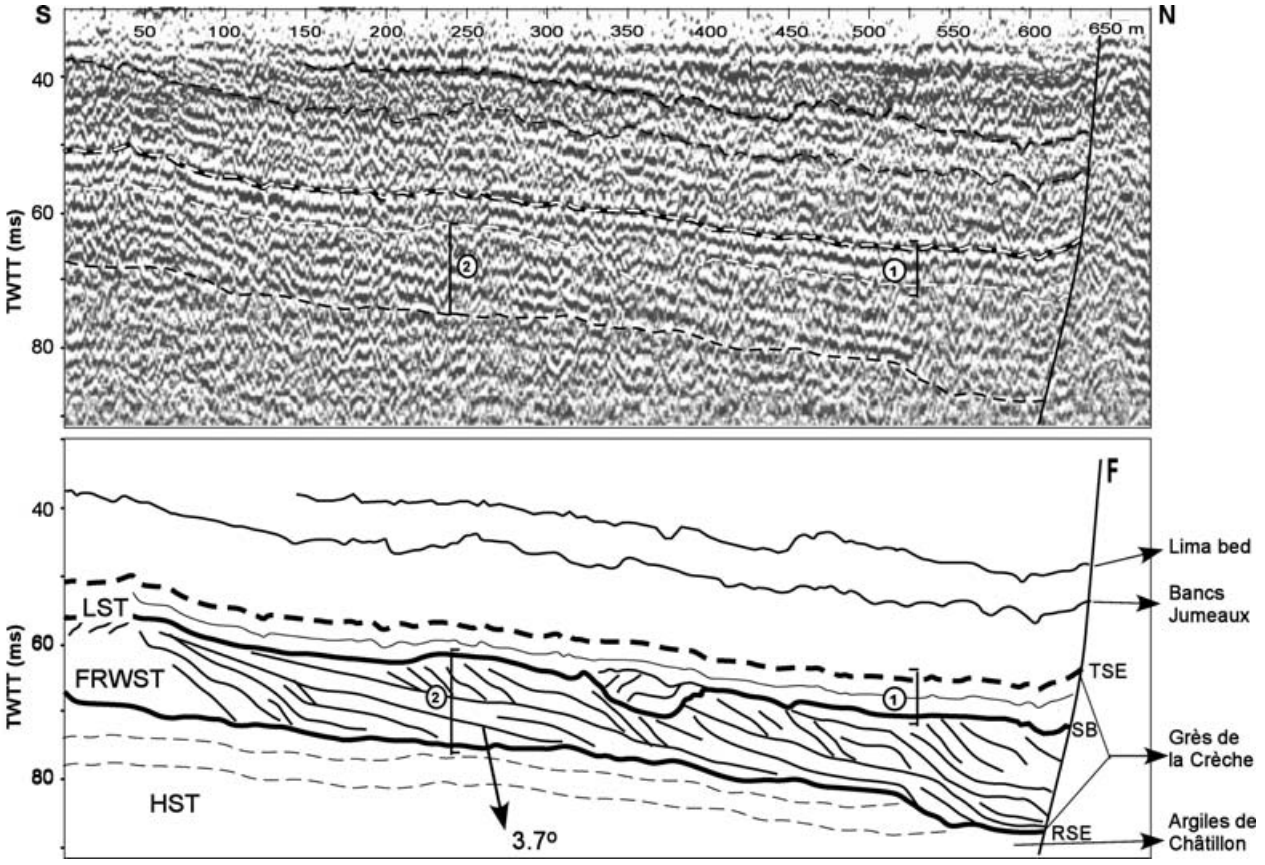

Figure 15 Offshore 2D sparker seismic reflection profile shot under rough weather conditions, located off Wimereux (see Figure 1 for location) and a line-drawing interpretation below. Peak frequency of the seismic line is approxately 450 Hz. The parallel continuous bundle of high-amplitude reflections (indicated by 1) is interpreted as the LST-part of the composite sharp-based shoreface deposit. The interval indicated 2 shows progradational geometries (the angle of prograding clinoforms is approximately 3.7°) and is interpreted as the FRWST-part of the composite sharp-based shoreface deposit (see text for discussion). RSE = regressive surface of marine erosion; SB = sequence boundary; TSE = transgressive surface of marine erosion.

during high-frequency sea-level oscillations, superimposed on an overall sea-level fall (forced regression). Consequently, the SB is characterized by repeated high-amplitude positive reflections when truncating a clinoform front and no reflections where it truncates uncemented FRWST sands (see Braaksma *et al*. 2006). A clear channel incision and fill can be observed at this surface around 375 m, backing up the purely sedimentological and log interpretation of this surface as a Type–1 sequence boundary.

At the base of its FRWST, the RSE also nearly retains amplitude over the full scale. It is frequency-dependent: towards 134 Hz, its amplitude gains strength, but from thereon it loses reflection-strength. This can be related to the presence of storm-related sandstone ribs and shell-beds below and the carbonate cemented sandstone bed above, which are destructively tuned with the RSE reflection. This example illustrates the complexity of extraction of geological information from lower-frequency seismic images only.

Nevertheless, when the frequency content of the seismic data can be extracted, and a sonic well log or acoustic core measurements are available, independently of the frequency content of the seismic data, a very accurate tie between seismic in time and geological information in depth can be made, and thus the origin and nature of seismic reflections can be determined. In addition, an alternative purely physical sequence stratigraphic interpretation on acoustic wireline logs and seismic reflection attributes can be made.

CONCLUSIONS

A quantitative relationship between geological parameters and their physical (seismic) expression was established by the extensive, multiscaled, high-resolution acquisition of both

geological and petrophysical parameters. Because of these combined efforts in the fields of geophysics, petrophysics and sedimentology, the following conclusions can be made for this natural observatory. These conclusions are expected to be more generally applicable.

1 Geostatistical analyses of granulometric (grain-size) facies, bulk carbonate content and acoustic properties provide a physical quantification of depositional environments, systems tracts and their key bounding surfaces across a complete depositional profile. The application of this physical sequence stratigraphic model quantifies the lateral continuity of petrophysical and geochemical parameters above and below these surfaces.

2 Numerical transmission and reflection experiments indicate that the transition from short-wavelength limits (ray theory) to long-wavelength limits (effective-medium theory) for the Boulonnais case study occurs at a λ/d-ratio of around 5.

3 To account for non-stationarity of the layered aspect of sedimentary deposits for traveltime predictions, a first-order correction on acoustic velocity through a medium can be found by applying an effective-medium-theory type of moving averaging with a window of one-fifth (as derived from conclusion 2) of the dominant wavelength.

4 Modulus maxima analyses on impedance contrasts of sonic logs acquired at different scales characterize the shape of the impedance contrasts (gradual, step or spike functions). This characterization is scale-dependent but can be directly linked to depositional environments, allowing extraction of geological information from seismic attributes.

5 The composite iterative upscaling method provides a nearly perfect tie of well to seismic and offers the possibility of determining the exact origin of seismic reflections, independently of the frequency content of seismic data sets. As a result, any seismic reflection can be correlated and ground-truthed by geological observations from logs and outcrop, beyond seismic resolution.

6 The surface seismic reflection survey design provided a seismic image with a resolution of nearly the intrinsic frequency of impedance layering (bedding rhythm).

7 Although reflection amplitudes become geologically more conspicuous at lower frequencies, the sharp-based shoreface deposits in the Boulonnais show a seismic reflection response typical for these kinds of deposits.

ACKNOWLEDGEMENTS

We thank all the students who helped with the acquisition of the seismic data set and sampling of the outcrops, and Bruis Gianotten and Klaas Verwer for their help with the data acquisition in France and in the petrophysics laboratory at the Vrije Universiteit in Amsterdam. We also thank TOTAL for funding the drilling of VUA-A, EGS (Luxembourg) for providing logging services and Geoffroy Mahieux for assisting in the core handling and logistics. Marc DeBatist and colleagues of RCMG, Gent, are acknowledged for the acquisition of, and their kindness in allowing us to use, the Bdb95004 seismic line in this paper. We thank Frédéric Verhelst for sharing his codes and Valentina Zampetti for constructive discussions. We thank Wolfgang Schlager for continuous support and peer reviews of this manuscript.

REFERENCES

Ahr W.M. 1973. The carbonate ramp: an alternative of the shelf model: Trans Gulf Coast. *American Geological Society* **23**, 221–225.

Anstey N.A. and O'Doherty R.F. 2002. Cycles, layers, and reflections: Part 1. *The Leading Edge* **21** (1), 44–51.

Banik N.C., Lerche I., Resnick J. and Shuey R.T. 1985b. Stratigraphic filtering part II: Model spectra. *Geophysics* **50**, 2775–2783.

Banik N.C., Lerche I. and Shuey R.T. 1985a. Stratigraphic filtering part I. Derivation of the O'Doherty-Anstey formula. *Geophysics* **50**, 2768–2774.

Berkhout A.J. 1982. *Seismic Migration: Imaging of Acoustic Energy by Wavefield Extrapolation:* Vol. A*: Theoretical Aspects*, 2nd ednEDZ, Vol. 14A Developments in Solid Earth Geophysics. Elsevier. Science Publishing Co.

Berkhout A.J. 1984. *Seismic Migration: Imaging of Acoustic Energy by Wavefield Extrapolation:* Vol. B*: Practical Aspects*, Vol. 14B Developments in Solid Earth Geophysics. Elsevier. Science Publishing Co.

Berkhout J.A. and Wapenaar C.P.A. 1990a. Delphi: Delft philosophy on acoustic and elastic inversion. *The Leading Edge* **9** (2), 30–33.

Berkhout J.A. and Wapenaar C.P.A. 1990b. Delphi: Delft philosophy on acoustic and elastic inversion, part 2. *The Leading Edge* **9** (3), 53–59.

Berner R.A. 1980. *Early Diagenesis; a Theoretical Approach*. Princeton University Press, Princeton, New Jersey.

Biddle K.T., Schlager W., Rudolph K.W. and Bush T.L 1992. Seismic model of a progradational carbonate platform, Picco di Vallandro, the Dolomites, northern Italy. *AAPG Bulletin* **76**, 14–30.

Blott J.S. and Pye K. 2001. Gradistat. A grain size distribution and statistics package for the analysis of unconsolidated sediments. *Earth Surface Processes and Landforms* **26**, 1237–1248.

Braaksma H., Kenter J.A.M., Proust J.N., Dijkmans V., van Hoek T., Mahieux G. and Drijkoningen G.G. 2003. Controls on acoustic properties of Upper Jurassic siliciclastic rocks (Boulonnais, northern France). *Geophysics* **68**, 58–69.

Braaksma H., Proust J.N., Kenter J.A.M., Drijkoningen G.G. and Filippidou N. 2006.

Bracco Gartner G.L. and Schlager W. 1999. Discrimination between onlap and lithologic interfingering in seismic models of outcrops. *AAPG Bulletin* **83**, 952–971.

Burchette T. and Wright V. 1992. Carbonate ramp depositional systems. *Sedimentary Geology* **79**, 3–57.

Carcione J.M., Kosloff D. and Behle A. 1991. Long-wave anisotropy in stratified media. *Geophysics* **56**, 245–254.

Carmichael R.S. 1990. *Practical Handbook of Physical Properties and Minerals*. CRC Press Incorporated, Boca Raton, Florida.

Curtis C.D. 1987. Inorganic chemistry and petroleum exploration. In. *Advances in Petroleum Geochemistry II* (eds Brooks. & D.Welte), pp. 91–140. Academic Press, Inc.

Dvorkin J. and Nur A. 1998. Time-average equation revisited: Short Note. *Geophysics* **63**, 460–464.

El Albani A., Deconinck J.F., Herbin J.P. and Proust J.N. 1993. Charactérisation géochimique de la matière organique et minérlogie des argiles du Kimmédridgien du Boulonnais. *Annals of Society Géological Nordiska* **2**, 113–120.

Gardner G.H.F., Gardner L.W. and Gregory A.R. 1974. Formation velocity and density, the diagnostic basis for stratigraphic traps. *Geophysics* **39**, 770–780.

Goudswaard J.C.M. 2001. *Multiangle multiscale characterization of seismic reflection data*. PhD Thesis. Delft University of Technology. ISBN 90-9015280-6.

Goudswaard J.C.M. and Wapenaar C.P.A. 2001. Scale and angle dependent reflection properties of self–similar interfaces. *Journal of Computational Acoustics* **9**, 1015–1023.

Goupillaud P., Grossmann A. and Morlet J. 1984. Cycle-octave and related transforms in seismic signal analysis. *Geoexploration* **23**, 85–102.

Grossmann A. and Morlet J. 1984. Decomposition of Hardy functions into square integrable wavelets of constant shape. *SIAM Journal of Mathematics* **15**, 723–736.

Guillocheau F., Robin C., Allemand P., Bourquin S., Brault N., Dromart G., Friedenberg R., Garcia J.P., Gaulier J.M., Gaumet F., Grosday B., Hanot F., Le Strat P., Mettreux M., Nalpas T., Prijac C., Rigollet C., Serrano O. and Grandjean G. 2000. Meso-Cenozoic geodynamic evolution of the Paris Basin: 3D stratigraphic constraints. *Geodinamica Acta* **13**, 189–246.

Hallam A. 1997. Estimates of the amount and rate of sea-level change across the Rhaetian-Hettangian and Pliensbachian-Toarcian boundaries (latest Triassic to early Jurassic). *Journal of the Geological Society (London)* **154**, 773–779.

Helbig K. 1984. Anisotropy and dispersion in periodically layered media. *Geophysics* **57**, 364–373.

Helland-Hansen W., Helle H.B. and Sunde K. 1994. Seismic modelling of Tertiary sandstone clinothems, Spitsbergen. *Basin Research* **6**, 181–191.

Herbin J.P., Fernandez-Martinez J.L., Geyssant J.R., El Albani A., Deconinck J.F., Proust. J.N., Colbeaux J.P. and Vidier J.P. 1995. Sequence stratigraphy of source rocks applied to the study of the Kimmeridgian/Tithonian in the north-west European shelf (Dorset, U.K., Yorkshire, U.K. and Boulonnais, France). *Marine and Petroleum Geology* **12**, 177–194.

Herrmann F.J. 1997. *A scaling medium representation, a discussion on well-logs, fractals and waves*. PhD Thesis. Delft University of Technology. ISBN 90-9010132-2.

Kennett B.L.N. 1974. Reflections, rays and reverberations. *Bulletin SeisMolecular Society America* **64**, 1685–1696.

Kenter J.A.M., Bracco Gartner G.L. and Schlager W. 2001. Seismic models of a mixed carbonate-siliciclastic shelf-margin: Permian Upper San Andres Formation, Last Change Canyon. *Geophysics* **66**, 1744–1748.

Kolla V., Biondi P., Long B. and Fillon R. 2000. Sequence stratigraphy and architecture of the Late Pleistocene Lagniappe delta complex, northeast Gulf of Mexico. In. *Sedimentary Responses to Forced Regression* (eds D. Hunt. & R. L. Gawthorpe), pp. 291–327. Geological Society London. Special Publication 172.

Levin F.K. 1979. Seismic velocities in transversely isotropic media. *Geophysics* **44**, 918–936.

Mahieux G., Proust J.N., Tessier B. and DeBatist M. 1998. Comparison between high-resolution seismic and sequence stratigraphic approaches applied to the Upper Jurassic deposits of the Dover strait area (Northern France). *Marine and Petroleum Geology* **15**, 329–342.

Mallat S. 1999. *A Wavelet Tour of Signal Processing*, 2nd edn. Academic Press Inc.

Mallat S. and Hwang W.L. 1992. Singularity detection and processing with wavelets. *IEEE Transactions on Information Theory* **38**, 617–643.

Mallat S. and Zang Z. 1993. Matching pursuit with time frequency dictionaries. *IEEE Transactions on Signal Processing* **41**, 3397–3415.

Mandelbrot B.B. 1974. Intermittent turbulence in self-similar cascades: divergence of high moments and dimension of the carrier. *Journal of Fluid Mechanics* **62**, 331–358.

Marion D., Mukerji T. and Mavko G. 1994. Scale effects on velocity dispersion: From ray to effective medium theories in stratified media. *Geophysics* **59**, 1613–1619.

Mavko G., Mukerji T. and Dvorkin J. 1998. *The Rock Physics Handbook: Tools for Seismic Analysis of Porous Media*. Cambridge University Press.

Melia P.J. and Carlson R.L. 1984. An experimental test of P-wave anisotropy in stratified media. *Geophysics* **49**, 374–378.

O'Doherty R.F. and Anstey N.A. 1971. Reflections on amplitude. *Geophysical Prospecting* **19**, 430–458.

Ogg J.G. 1995. Phanerozoic magnetic polarity time scale. *Global EarthPhysics, A Handbook of Physics Constants*, pp. 240–270. AGU reference Shelf 1.

Oschmann W. 1988. Kimmeridge clay sedimentation – a new cyclic model. *Palaeogeography, Palaeoclimatology, Palaeoecology* **65**, 217–251.

Oschmann W. 1990. Environmental cycles in the Late Jurassic northwest European epeiric basin: interaction with atmospheric and hydrospheric circulations. *Sedimentary Geology* **69**, 313–332.

Posamentier H.W., Allen G.P., James D.P. and Teeson M. 1992. Forced regressions in a sequence stratigraphic framework: concepts, examples, and exploration significance. *AAPG Bulletin* **76**, 1687–1709.

Posamentier H.W. and Chamberlain C.J. 1993. Sequence stratigraphic analysis Viking Formation lowstand beach deposits at Joarcam Field, Alberta, Canada. In. *Sequence Stratigraphy and Facies Associations* (eds H. W. Posamentier, C. P. Summerhayes, B. U. Haq. & G. P. Allen), pp. 469–485. International Association of Sedimentologists. Special Publication 18.

Posamentier H.W. and Morris W.R. 2000. Aspects of the stratal architecture of forced regressive deposits. In. *Sedimentary Responses to Forced Regression* (eds D. Hunt. & R. L. Gawthorpe), pp. 19–46. Geological Society London. Special Publication 172.

Proust J.N., Deconinck J.F., Geyssant J.R. and Herbin J.P. 1993. and. Vidier J.P Nouvelles données sédimentologiques dans le Kimmeridgien et le Tithonien du Boulonnais (France). *C Royal Academy of Science Paris* **316**, II, 363–369.

Proust J.N., Deconinck J.F., Geyssant J.R., Herbin J. P. and Vidier J.P. 1995. Sequence analytical approach to the Upper Kimmeridgian-Lower Tithonian storm-dominated ramp deposits of the Boulonnais (Northern France). A landward time equivalent to offshore marine source rocks. *Geologische Rundschau* **84**, 255–271.

Proust J.N., Mahieux G. and Tessier B. 2001. Field and seismic images of sharp-based shoreface deposits: Implications of sequence stratigraphic analysis. *Journal of Sedimentary Research* **71**, 944–957.

Purkis S.J. 2004. *Calibration of Satellite Images of Reef Environment*. PhD Thesis, Vrije Universiteit, Amsterdam. ISBN 90-9017043-5.

Read J.F. 1985. Carbonate platform facies model. *AAPG Bulletin* **69**, 1–21.

Rio P., Mukerji T., Mavko G. and Marion D. 1996. Velocity dispersion and upscaling in a laboratory-simulated VSP. *Geophysics* **61**, 584–593.

Rudolph K.W., Schlager W. and Biddle K.T. 1989. Seismic models of carbonate foreslope-to-basin transition, Picco di Vallandro, Dolomite Alps, northern Italy. *Geology* **17**, 453–456.

Sams M.S. and Williamson P.R. 1994. Backus averaging, scattering and drift. *Geophysical Prospecting* **42**, 541–564.

Schlager W. 2004. Fractal nature of stratigraphic sequences. *Geology* **32**, 185–188.

Sengbush R.L., Lawrence P.L. and McDonald F.J. 1961. Interpretation of synthetic seismograms. *Geophysics* **26**, 138–157.

Shapiro S.A. and Zien H. 1993. The O'Doherty-Anstey formula and localization of seismic waves. *Geophysics* **58**, 736–740.

Stafleu J. and Schlager W. 1993. Pseudo-toplap in seismic models of the Schlern-Raibl contact (Sella platform, northern Italy). *Basin Research* **5**, 55–65.

Taner M.T., Koehler F. and Sheriff R.E. 1979. Complex seismic trace analysis. *Geophysics* **44**, 1041–1063.

Taylor K.G., Gawthorpe R.L., Curtis C.D., Marschall J.D. and Awwiller D.N. 2000. Carbonate cementation in a sequence-stratigraphic framework: upper Cretaceous sandstones, Book Cliffs, Utah-Colorado. *Journal of Sedimentary Research* **70**, 360–372.

Taylor S.P. and Sellwood B.W. 2002. The context of lowstand events in the Kimmeridgian (Late Jurassic) sequence stratigraphic evolution of the Wessex-Weald Basin, southern England. *Sedimentary Geology* **151**, 89–106.

Tesson M., Gensous B., Allen G.P. and Ravenne C. 1990. Late Quaternary deltaic lowstand wedges on the Rhone continental shelf, France. *Marine Geology* **19**, 325–332.

Thomson L. 1986. Weak elastic anisotropy. *Geophysics* **51**, 1954–1966.

Tribovillard N., Bialkowski A., Tyson R.W., Lallier-Verges E. and Deconinck J.F. 2001. Organic facies variations in the Late Kimmeridgian of the Boulonnais area (northernmost France). *Marine and Petroleum Geology* **18**, 371–389.

Van Wagoner J.C., Posamentier H.W., Mitchum R.M., Vail P.R., Sarg J.F., Loutit T.S. and Hardenbol J. 1988. An overview of the fundamentals of sequence stratigraphy and key definitions. In: *Sea-Level Changes An Integrated Approach* (eds C. K. Wilgus, B. S. St. Hastings, C. G. C. Kendall, H. W. Posamentier, C. A. Ross, J. C. Van Wagoner), pp. 39–45. Society Economic Paleontologists and Mineralogists. Special Publication 42.

Verhelst F. 1998. Local wavelet attributes (amplitude, phase and scale) for geological characterization. 68th SEG Meeting, New Orleans, USA, Expanded Abstracts, 624–627.

Verhelst F. 2000. *Integration of seismic data with well-log data*. PhD Thesis. Delft University of Technology. ISBN 90-9014386-6.

Vermeer P.L. and Alkemaade J.A.H. 1992. Multiscale segmentation of well logs. *Mathematical Geology* **24**, 27–44.

Vernik L. and Nur A. 1992. Petrophysical classification of siliciclastics for lithology and porosity predictions from seismic velocities. *AAPG Bulletin* **76**, 1295–1309.

Volker A.W.F., Duijndam A.J.W., Blacquiere G. and Berkhout A.J. 2000. Analysis and optimization of 3-D acquisition geometries by focal beams. 70th SEG Meeting, Calgary, Canada, Expanded Abstracts, 68–71.

Widess M.B. 1973. How thin is a thin bed? *Geophysics* **38**, 1176–1180.

Wignall P.B. 1989. Sedimentary dynamics of the Kimmeridge clay: tempests and earthquakes. *Journal of the Geological Society (London)* **146**, 273–284.

Wignall P.B. 1991. *Test of the Concepts of Sequence Stratigraphy in the Kimmeridgian* (late Jurassic) of England and northern France. Marine and Petroleum Geology 8, 430–441.

Wignall P.B. and Newton R. 2001. Black shales on the basin margin: a model based on examples from the Upper Jurassic of the Boulonnais, northern France. *Sedimentary Geology* **144**, 335–356.

Wignall P.B., Sutcliffe O.E., Clemson J. and Young E. 1996. Unusual shoreface sedimentology in the upper Jurassic of the Boulonnais, northern France. *Journal of Sedimentary Research* **66**, 577–586.

Williams C.J., Hesselbo S.P., Jenkyns H.C. and Morgans-Bell H.S. 2001. Quartz silt in mudrocks as a key to sequence stratigraphy (Kimmeridge Clay Formation, Late Jurassic, Wessex basin, UK). *Terra Nova* **13**, 449–455.

Wyllie M.R.J., Gregory A.R. and Gardner G.H.F. 1956. Elastic wave velocities in heterogeneous and porous media. *Geophysics* **21**, 41–70.

Zeng H. and Kerans C. 2003. Seismic frequency control on carbonate seismic stratigraphy: a case study of the Kingdom Abo sequence, west Texas. *AAPG Bulletin* **83**, 273–293.

Ziolkowski A., Underhill J.R. and Johnston R.G.K. 1998. Wavelets, well ties, and search for subtle stratigraphic traps. *Geophysics* **63**, 297–313.

Zoeppritz K. 1919. Erdbebenwellen VII. VIIb. Über Reflexion und Durchgang seismischerWellen durch Unstetigkeitsflächen. Nachrichten der Königlichen Gesellschaft der Wissenschaften zu Göttingen, Mathematisch-physikalische Klasse, 66–84.